Texas A&M University
Mechanical Engineering Department
Turbomachinery Laboratory
Tribology Group

THERMO HYDRODYNAMIC (THD) COMPUTATIONAL ANALYSIS FOR TILTING PAD THRUST BEARINGS (TPTBS)

TRC-B&C-05-17

A Report to the Turbomachinery Research Consortium

By

Luis San Andrés
Mast-Childs Chair Professor
Principal Investigator

Rasool Koosha
Research Assistant

May 2017

EXECUTIVE SUMMARY

Thermo-Hydrodynamic (THD) Computational Analysis For Tilting Pad Thrust Bearings (TPTBs)

Hydrodynamic thrust bearings (TBs) control rotor position in rotating machinery. Tilting pad thrust bearings (TPTBs), consume less power and show a lesser temperature rise than those in rigid surface bearings. The Turbomachinery Laboratory funded a one-year effort to offer TRC members a sound choice for the engineered design of TPTBs. The report details a thermo-hydrodynamic (THD) analysis for the static and dynamic force performance of TPTBs. The goal is to deliver a modern predictive tool for TPTBs to be further integrated into the XLTRC^{2}software suite.

The model couples a generalized Reynolds equation for the film pressure, including cross-film viscosity variation and turbulent flow effects, a 3D thermal energy transport equation for the film temperature, and a heat conduction equation for pad temperature. Numerical solution of the governing equations with approximate boundary conditions delivers pressure and temperature fields toward the calculation of a TPTB load capacity, shear drag power loss, and required flow rate. A small amplitude thrust collar motion (perturbation) analysis produces first-order pressure fields to calculate the bearing axial stiffness and damping (frequency reduced) coefficients.

To check the accuracy of the model, predictions are benchmarked versus archival test data for a six-pad TPTB (228 mm OD) under specific load of 0.5 to 2.0 MPa and operating with rotor speed of 1.5 to 3.0 krpm (36 m/s). The predictions of the current THD model are in a good agreement with the test data with a maximum difference of 8% for pressure field, 17% for pad temperature, 20% for fluid film thickness, and 8% for power loss.

TABLE OF CONTENTS

LIST OF FIGURES

LIST OF TABLES

NOMENCLATURE

c_P	Lubricant specific heat [J/kg ˚C]
C_{XY}	Fluid film damping coefficients (X=z, γ, ξ and Y = e_c, e_p, α, β)
C_{XYs}	Pivot damping coefficients (X=η, γ, ξ and Y = e_p, α, β)
e_c	Axial location of thrust collar [m]
e_P	Axial location of pivot tip [m]
f, g	Turbulence functions, Eqn. (48)
F_z	Fluid film axial force acting on the thrust collar [N]
F_η	Fluid film axial force acting on a pad [N]
G, H_r, H_θ	Turbulence functions, Eqns. (3) to (5)
h	Fluid film thickness [m]
I_γ, I_ξ	Pad mass moments of inertia with respect to (γ,ξ) axes [kg.m^2]
K_{XY}	Fluid film stiffness coefficients (X=z, γ, ξ and Y = e_c, e_p, α, β)
K_{XYs}	Pivot stiffness coefficients (X=η, γ, ξ and Y = e_p, α, β)
m	Pad mass [kg]
M_γ, M_ξ	Fluid film radial and circumferential moments acting on a pad [N.m]
N	Shaft rotational speed [rpm], N=$\Omega\pi$/30
N_p	Number of pads in a TPTB
P	Pressure [Pa]
Q	flowrate [LPM]
R_{in}, R_{out}	Inner radius and outer radius of a pad [m]
(R_P, θ_P)	Radial and circumferential location of pivot in global coordinate system [m]
t_p	Pad thickness [m]
t	Time
T	Fluid film temperature [˚C]
T_p	Pad temperature [˚C]
T_*	Supply temperature [˚C]
W_z	Applied axial load [N]
$\hat{z}$	Axial coordinate cross the fluid film thickness [m]
Z_{XY}	Fluid film complex stiffness coefficients (X=z, γ, ξ and Y = e_c, e_p, α, β)
Z_{XYs}	Pivot complex stiffness coefficients (X=η, γ, ξ and Y = e_p, α, β)
(α, β)	Pad tilt angles around (γ, ξ) axes[rad]
α_{TV}	Lubricant temperature-viscosity coefficient [1/˚C]
ϵ_m	Eddy viscosity for momentum [m^2/s]
θ_t	Circumferential location of trailing edge in global coordinate system [rad]
θ_l	Circumferential location of leading edge in global coordinate system [rad]
λ	Heat convection coefficient [W/m^2˚C]
μ	Lubricant dynamic viscosity [Pa.s]
ν	Lubricant kinematic viscosity (cSt)
ρ	Lubricant density [kg/m^3]
κ	Lubricant conductivity coefficient [W/m C]
κ_p	Pad material conductivity coefficient [W/m C]
Ω	Shaft angular speed [rad/s]
ω	Excitation frequency [rad/s]

Matrices

C	Damping coefficient matrix
K	Stiffness coefficient matrix
Z	Complex stiffness coefficient matrix

Subscript

a	Ambient
h	Bearing housing
in	Inner radius
l	Leading edge
out	Outer radius
p	Pad
P	Pivot
t	Trailing edge
*	Supply

Coordinate Systems

(x,y,z)	Global Cartesian coordinate system, originate at the center of bearing housing surface
(r,θ,z)	Global Cylindrical coordinate system, originate at the center of bearing housing surface
(γ,ξ,η)	Pad local Cartesian coordinate system, originate at pivot tip and constrained to move with it.

Abbreviation

FEM	Finite Element Method
FDM	Finite Difference Method
TEHD	Thermo-elasto-hydrodynamic Analysis
THD	Thermo-hydrodynamic Analysis
TPTB	Tilting Pad Thrust Bearing

INTRODUCTION

Tilting Pad Thrust Bearings (TPTBs) are used in rotating machinery to control rotor axial placement. Their main advantages are low power loss, simple installation, and low-cost maintenance. Figure 1 depicts a schematic view of a TPTB (the fluid film thickness and pad tilts are exaggerated for clarity), consisting of a bearing housing, a thrust collar attached to the rotating shaft, and a series of pads supported on pivots. The ports in the bearing housing supply cold lubricant into the bearing pads, meanwhile some hot lubricant leaves the bearing through its sides. In the grooves between pads, the cold supplied lubricant mixes with the upstream hot flow and enters the leading edge of the downstream pad. As the thrust collar rotates, it draws the fluid into the wedge (between a pad and the collar) to generate a hydrodynamic pressure field. Lubricant is sheared through the hydrodynamic wedge and its temperature increases. The load capacity of a hydrodynamic fluid film bearing largely depends on the lubricant viscosity, a function of its temperature.

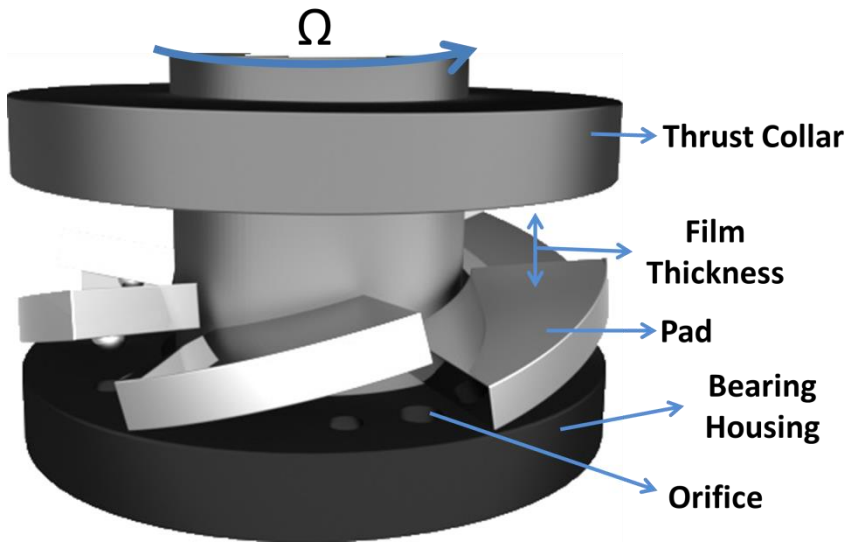

Figure 1. Schematic view of a tilting pad thrust bearing (Film thickness and pad tilts exaggerated).

Modern rotating machinery demands for the improved design of fluid film bearings to operate with higher shaft speeds and withstand heavier loads. An accurate predictive tool is a key to design thrust bearings without resorting to (expensive and time consuming) testing. In 1996, San Andrés and Zirkelback [1] introduce a computational analysis tool for fixed-geometry laminar flow TBs, using a lump thermal model for fluid temperature rise. To date, the "Thrust"

program developed by the ROMAC group [2] at the University of Virginia is a popular predictive tool for laminar flow and turbulent flow TPTBs. This tool performs a thermo-elasto-hydrodynamic analysis (TEHD) and accounts for cross-film viscosity variation and thrust collar misalignments, and delivers 3D temperature distribution in the fluid film, pads, and thrust collar; as well as elastic deformations of both pads and the thrust collar [2].

In 2016, the Turbomachinery Laboratory made a strategic investment ($25 k) to develop a predictive tool for hydrodynamic thrust bearings, tilting type. The computational tool should serve TRC members' need of a modern predictive tool, further integrated into the XLTRC^2 software suite. Analysis of tilting pad journal bearings (TPJBs) has reached great complexity as 3D computational fluid dynamics models are coupled to finite element structural models for the pads, journal and bearing housing, and also account for fluid-solid interaction. A similar effort should also aim to better model TPTBs.

The current report details a thermo-hydrodynamic (THD) model for analysis of TPTBs that includes a 3D (cross-film) thermal energy transport equation and a model for turbulent flow in the Reynolds equation for the generation of hydrodynamic pressure. A conduction heat transfer equation couples the temperature field in a pad to the temperature field in the fluid film. The model also includes a perturbation analysis with axial displacement of the thrust collar to determine the bearing axial stiffness and damping force coefficients.

Validation of the THD model correlates predictions to test data in Refs.[3,4]. At the current state, a conventional thermal mixing model in a feed port estimates the fluid temperature at the leading edge of a pad. A nonlinear model is also included for pivot stiffness. The model assumes identical operating fluid film thickness for all pads (no collar misalignments). The current computational tool, predicting the film thickness due to an applied load, the hydrodynamic pressure field, and 3D temperature distribution in the fluid film and in a pad, delivers performance parameters including drag torque, power loss, flow rate, and (frequency reduced) axial force coefficients.

1. REVIEW OF PAST WORK

The works of Jeng et al. [5–7] at the University of Pittsburgh (1986), Brockett et al. [8] at the University of Virginia (1996), and Glavatskih et al. [9] at Lulea University of Technology (2004) are representative of thrust bearings analysis . Table 1 outlines the characteristics of these models.

Table 1. Comparison between different approaches for thrust bearing modeling

Author		Jeng et al. [5–7]	Brockett et al. [8]	Glavatskih et al. [9]
Year		1986	1996	2004
Analysis		THD	TEHD	TEHD
Hydrodynamic analysis		2D pressure field	2D pressure field	2D pressure field
Thermal analysis	Equations	- 3D energy transport equation in the fluid film - 1D heat transfer equation in a pad (cross the pad thickness)	- 3D energy transport equation in the fluid film - 3D heat conduction equation in a pad - 2D axisymmetric heat conduction equation in the thrust collar	- 3D energy transport equation in the fluid film - 3D heat conduction equation in a pad - 2D axisymmetric heat conduction equation in the thrust collar
	Boundary conditions	- Adiabatic condition at thrust collar surface - Heat flux at pad surfaces (top and bottom)	- Heat flux at thrust collar surfaces - Heat flux at pad surfaces	- Heat flux at thrust collar surfaces - Heat flux at pad surfaces
	Results	- 3D temperature distribution in the fluid film - 3D temperature distribution in a pad	- 3D temperature distribution in the fluid film - 3D temperature distribution in a pad - 2D axisymmetric temperature distribution in the thrust collar	- 3D temperature distribution in the fluid film - 3D temperature distribution in a pad - 2D axisymmetric temperature distribution in the thrust collar.
Elasticity analysis		Disregarded	- 3D pad deformations (thermal and mechanical) - 2D thrust collar axisymmetric deformations (mechanical)	- 3D pad deformations (thermal and mechanical).
Turbulence effects		Ng's model	Disregarded	Disregarded
Groove thermal mixing		Disregarded	A conventional model	A conventional model
Experimental Validation		NA	NA	Conducted

The following provides more detailed description on the theoretical analysis of TPTBs.

Jeng et al. [5–7]:

In 1986, Jeng et al. [5] adopt a model (Ng's model of turbulent flow [10]) to account for turbulent flow effects in TPTB analysis. A generalized Reynolds equation extends earlier analysis (bulk flow model of Hirs 1974 [11]) to include viscosity variation cross the fluid film thickness. Solution of a thermal energy transport equation in the fluid film, coupled to a 1D (across pad thickness) heat conduction equation, delivers 3D temperature distribution and further leads to a cross-film viscosity variation. The authors present predictions for a turbulent flow TPTB with a diameter of 2.8 m operating with a rotor speed of 3 krpm (mean surface speed of ΩR_m=354 m/s). Predictions are not compared against test data.

In a second part, Jeng et al. [6] include surface spherical crowning to approximate the shape of a deformed pad due to the combine action of pressure and temperature. For the same TPTB, operating with a rotor speed of 390 rpm (ΩR_m=41 m/s) when the thrust collar is fixed with a 60 μm clearance from pads (at pivot), the authors notice fluid film cavitation near the trailing edge. Accounting for pad deformation significantly improves prediction for load capacity, but predictions for fluid film maximum temperature (oil exit temperature) show large discrepancies with experimental data (13 ˚C equal to 25% of the temperature rise).

In a third part, Jeng et al. [7], using Euler's equation for a pad rotational modes, pioneer a model to predict the axial force coefficients ([*K, C*]) for a turbulent flow TPTB. The authors assume a rigid pivot and disregard pad's translational modes. A parametric study, for the same TPTB operating with a rotor speed of 3 krpm (ΩR_m=354 m/s) and with a clearance of 60 μm (at pivot), shows that excitation frequency and pad mass have respectively no significant effect and little significant effect on bearing force coefficients ([*K, C*]). On the other hand, temperature dependency of the fluid viscosity and pad deformations show strong impact on bearing force coefficients.

In general, the THD analysis presented by Jeng et al. [5–7] remains a popular model for turbulent flow TPTBs. However, this model disregards heat convection through thrust collar surfaces and pad side surfaces. In a more recent study (2012), Wodtke et al. [12] observe that heat convection has a significant impact on the performance predictions of a TPTB. Moreover, the presented model does not include a thermal mixing model in the grooves between pads and, the temperature of the fluid film inlet flow is assumed equal to supply temperature. In two

distinct studies, Wasilczuk and Rotta (2008) [13] and San Andrés and Abdollahi (2017) [14] point out that the static and dynamic force performance of a fluid film bearing (thrust bearing and journal bearing, respectively) are largely determined by the fluid temperature at the leading edge of a pad, which is directly governed by thermal mixing phenomena in a groove.

Brocket et al. [8]:

In 1996, Brockett et al. [8] develop a thermo-elasto-hydrodynamic (TEHD) model for laminar flow fixed geometry thrust bearings. Brocket et al. include a 3D heat conduction equation in a pad and an axisymmetric heat conduction equation in the thrust collar. The authors also account for 3D elastic deformations of a pad due to mechanical (pressure) and thermal (temperature) loading as well as axisymmetric elastic deformation of the thrust collar due to only mechanical loading. A study, for a six-pad TB with 305 mm in diameter operating with a rotor speed of 2 krpm (ΩR_m=26.6 m/s) and under a specific load between 1.32 to 10.52 MPa, shows that heat convection to pads has a large influence on the bearing performance at higher loads (>8 MPa) and adiabatic condition is only valid for lower loads (>5 MPa). Allowing heat flux to determine the temperature of the thrust collar decidedly changes predictions, compared to predictions made assuming isotherm thrust collar. Comparing predictions obtained with and without accounting for elastic deformations in a pad shows that mechanical deformation is small (8% of h_{min}) and leads to a maximum temperature rise of 2 °C whereas thermal deformation is relatively large (45% of h_{min}) and could cause a maximum temperature rise up to 24 °C. Power loss and flow rate are insignificantly (at most, 8%) affected by deformation modes. Predictions of the presented TEHD analysis are not compared against experimental data.

Glavatskih et al.[3,15,16]:

In 1999, Almqvist et al. [3], in a more detailed THD analysis for laminar flow TPTBs (including thermal analysis in pads and the thrust collar), adopt a conventional thermal mixing model for pad inlet flow. The authors compare predictions and measured data for a six-pad laminar flow TPTB with 228 mm in diameter, operating with a rotor speed between 1.2 to 2.5 krpm (ΩR_m=11-23 m/s) and under a specific load between 0.5 to 2.0 MPa. Predictions differ from test data up to 20% for pressure, up to 10 % for thrust collar temperature, and up to 10% for

power loss.

Two years later, Glavatskih et al. [15] extend the above model to account for both pressure and temperature induced elastic deformations of pads. Predictions are compared against test data for the same TPTB operating with rotor speed up to 3 krpm (ΩRm=28 m/s), and under a specific load up to 2.0 MPa. TEHD predictions for pad temperature show up to15% improvement over predictions delivered by THD analysis.

In 2002, Glavatskih et al. [16] include a new model to the TEHD analysis above for the flow temperature at the leading edge of a pad. The new model determines the inlet temperature by applying the energy conservation equation and accounting for the imposed lubricant flow rate and the total flow of hot lubricant carried out from the sides and trailing edge. Predictions are compared to test data for the same TPTB operating with 3 krpm (ΩR_m=28 m/s) and under a specific load of 2.0 MPa. Predictions differ from test data up to 16% for power loss, pad temperature, and fluid film thickness. Generally, the new model does not lead to more accurate predictions, compared to the previous conventional model. However, the main advantage is that the new model does not rely on a carry-over thermal mixing coefficients.

In a second part, Glavatskih et al. perform a parametric study to evaluate the impact of pad initial surface crowning (unloaded) on the operating performance of a TPTB. Benchmarking predictions versus test data, for the same TPTB operating with 3 krpm (ΩR_m=28 m/s) and under a specific load of 2.0 MPa, shows that predictions are improved up to 17% (12 μm) for fluid film thickness. Improvements for temperature and pressure are marginal. The authors believe that improvements occur since a pad surface is practically never flat due to machining tolerances. However, these improvements might indicate that pad deformations have been underestimated by theory. In general, Glavatskih et al. observe that surface crowning more significantly influences the leading edge film thickness (h_{max}) than the trailing edge film thickness (h_{min}).

Up to date, the TEHD predictive tool presented by Glavatskih et al. [17] includes the most comprehensive thermal analysis for laminar flow TPTBs. However, this model comes up short to account for elastic deformations in the thrust collar, to include an accurate model for thermal mixing in grooves, and to predict dynamic force coefficients.

A more recent work:

In 2010, Ahmed et al. [18] use a TEHD analysis tool to study the impact of elastic deformations of pads and the thrust collar on the performance of a fixed-geometry hydrodynamic TB. Their model accounts for pad deformations due to both pressure and temperature changes and the thrust collar deformations only due to pressure changes. Predictions for an eight-pad thrust bearing with 200 mm in diameter, operating with a rotor speed of 2.6 krpm (ΩR_m=21 m/s), and under a specific load of 1.4 MPa shows that pad mechanical deformations do not exceed 5 μm and have a very limited influence on the fluid film thickness. On the other hand, the pressure induced deformations in the thrust collar raise up to 45 μm and significantly influence the film thickness. The predictions made by the TEHD model largely differ from THD predictions as the applied load increases (>0.9 MPa). The maximum difference is 8% for pressure (0.4 MPa), 40% for film thickness (15 μm), and 20% for fluid film temperature rise (6 °C).

The current work reaches out to Refs. [3–5], for fundamentals in turbulent flow TPTBs analysis, including the solutions of Reynolds equation, thermal energy transport equation, and pad heat conduction equation, to build a THD computational tool for static and dynamic force performance of TPTBs.

2. ANALYSIS

The following details a thermo-hydrodynamic analysis for TPTBs. Note that the model assumes identical operating fluid film thickness for all pads in a TPTB (no thrust collar misalignment). Hence, this report details analysis only for one pad.

Figure 2 depicts a pad geometry and the definition of variables in a TPTB. A cylindrical coordinate system (r,θ,z) has its origin at the center of bearing housing surface (O_B) with the z-axis normal to its surface. Let (γ,η,ξ) represent a system of body axis which is originated at the pivot tip and constrained to move with it. The γ-axis and η-axis are parallel to (y,z) axes, respectively, and, the ξ-axis is extended in the opposite direction of the x-axis.

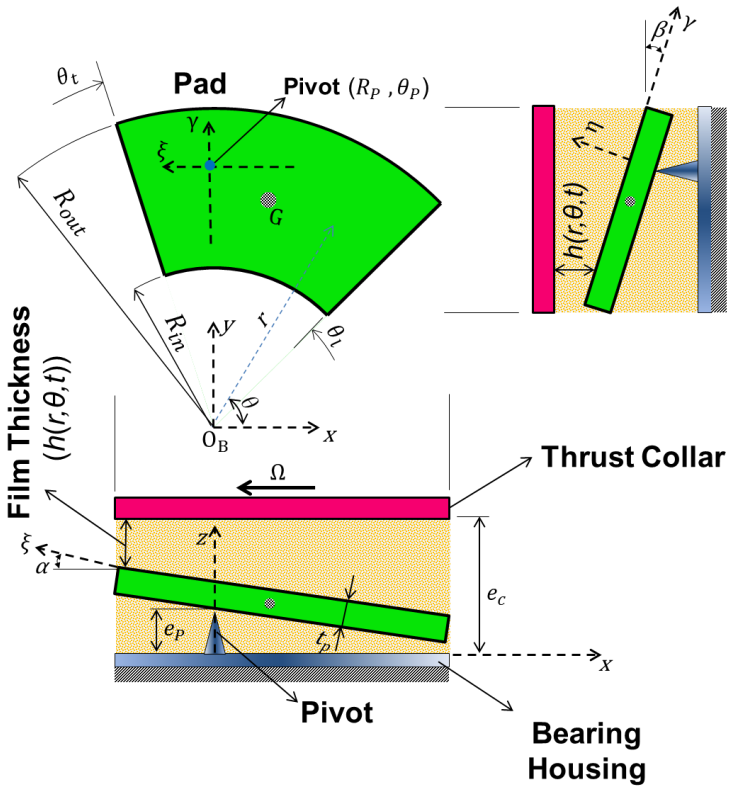

e_P	Pivot axial location
e_c	Thrust collar axial location
G	Pad mass center
h	Film thickness
O_B	Bearing housing center point
(r,θ,z)	Global cylindrical coordinate system
R_P	Pivot radial location
R_{in}	Inner radius
R_{out}	Outer radius
t_p	Pad thickness
(x,y,z)	Global Cartesian coordinate system
α	Pad radial tilt angle
β	Pad circumferential tilt angle
(γ, ξ,η)	Local Cartesian coordinate system
θ_P	Pivot circumferential location
θ_t	Trailing edge circumferential location
θ_l	Leading edge circumferential location
Ω	Shaft rotational speed

Figure 2. Geometry and coordinate systems for a pad in a TPTB.

At any point on a pad surface, the film thickness ($h_{(r,\theta,t)}$) is a function of the thrust collar axial location ($e_{c(t)}$), the pivot axial location ($e_{P(t)}$), and the pad tilt angles ($\alpha_{(t)}$,$\beta_{(t)}$), respectively around (γ,ξ) axes. On a pad with a pivot located at (R_P,θ_P) the film thickness is,

$$h_{(r,\theta,t)} = (e_c - e_P - t_p) + \alpha\left(r\sin\left(\theta_p - \theta\right)\right) + \beta\left(r\cos\left(\theta_P - \theta\right) - R_P\right) \tag{1}$$

where t_p is the pad thickness.

2.1 Reynolds Equation for a Thin Film

Jeng et al. [5] derive a general form of the Reynolds equation governing the generation of hydrodynamic pressure field ($P_{(r,\theta,t)}$) in a turbulent flow fluid film bearing. The fluid is Newtonian, incompressible, and inertialess. This equation is [5]

$$\frac{1}{r}\frac{\partial}{\partial r}\left(rH_r\frac{\partial P}{\partial r}\right) + \frac{1}{r}\frac{\partial}{\partial \theta}\left(H_\theta\frac{1}{r}\frac{\partial P}{\partial \theta}\right) = \Omega\frac{\partial G}{\partial \theta} + \frac{\partial h}{\partial t} \tag{2}$$

where Ω is the rotor (thrust collar) rotational speed, and (H_r, H_θ, and G) are turbulent flow functions defined as, [5]

$$H_{r(r,\theta,t)} = \int_0^h\left(\int_0^{\hat{z}}\xi_3(\delta)\,d\delta\right)d\hat{z} - \frac{\int_0^h\xi_3(\hat{z})\,d\hat{z}}{\int_0^h\xi_4(\hat{z})\,d\hat{z}}\int_0^h\left(\int_0^{\hat{z}}\xi_4(\delta)\,d\delta\right)d\hat{z} \tag{3}$$

$$H_{\theta(r,\theta,t)} = \int_0^h\left(\int_0^{\hat{z}}\xi_1(\delta)\,d\delta\right)d\hat{z} - \frac{\int_0^h\xi_1(\hat{z})\,d\hat{z}}{\int_0^h\xi_2(\hat{z})\,d\hat{z}}\int_0^h\left(\int_0^{\hat{z}}\xi_2(\delta)\,d\delta\right)d\hat{z} \tag{4}$$

$$G_{(r,\theta,t)} = h - \frac{1}{\int_0^h\xi_4(\hat{z})\,d\hat{z}}\int_0^h\left(\int_0^{\hat{z}}\xi_4(\delta)\,d\delta\right)d\hat{z} \tag{5}$$

Above, ξ_i , $i = 1{:}4$ are functions of the local viscosity (μ) across the fluid film and the flow turbulence. Appendix A details the ξ functions. Note that, in a laminar flow with constant viscosity cross the fluid film,

$$H_r = H_\theta = \frac{h^3}{12\mu}, \quad G = \frac{h}{2} \tag{6}$$

then, the Reynolds equation takes a familiar from,

$$\frac{1}{r}\frac{\partial}{\partial r}\left(r\frac{h^3}{12\mu}\frac{\partial P}{\partial r}\right) + \frac{1}{r}\frac{\partial}{\partial \theta}\left(\frac{1}{r}\frac{h^3}{12\mu}\frac{\partial P}{\partial \theta}\right) = \frac{\Omega}{2}\frac{\partial h}{\partial \theta} + \frac{\partial h}{\partial t} \tag{7}$$

Let (*U,V,W*) be the radial, circumferential, and axial components of the fluid velocity, respectively, induced by pressure gradient and thrust collar rotation. Jeng et al. [5] state them as,

$$U_{(r,\theta,\hat{z},t)} = -\frac{\partial P}{\partial r}\left[\int_0^{\hat{z}}\xi_3(\delta)d\delta - \frac{\int_0^h \xi_3(\delta)d\delta}{\int_0^h \xi_4(\delta)d\delta}\int_0^{\hat{z}}\xi_4(\delta)d\delta\right] \tag{8}$$

$$V_{(r,\theta,\hat{z},t)} = r\Omega\left[\frac{\int_0^{\hat{z}}\xi_4(\delta)d\delta}{\int_0^h \xi_4(\delta)d\delta}\right] - \frac{1}{r}\frac{\partial P}{\partial \theta}\left[\int_0^{\hat{z}}\xi_1(\delta)d\delta - \frac{\int_0^h \xi_1(\delta)\,d\delta}{\int_0^h \xi_2(\delta)\,d\delta}\int_0^{\hat{z}}\xi_2(\delta)d\delta\right] \tag{9}$$

$$W_{(r,\theta,\hat{z},t)} = -\int_0^{\hat{z}}\frac{U}{r}d\delta - \int_0^{\hat{z}}\frac{\partial U}{\partial r}d\delta - \int_0^{\hat{z}}\frac{1}{r}\frac{\partial V}{\partial \theta}d\delta \tag{10}$$

where $\hat{z} = 0$ at a pad surface and $\hat{z} = h$ at the collar surface.

2.2 The Fluid Flow Thermal Energy Transport Equation

The thermal energy transport equation balances between the energy generated due to viscos shear dissipation in the fluid and the energy disposed through fluid advection and conduction to the solids (pads and the thrust collar). Figure 3 shows a schematic view of the fluid film boundary conditions.

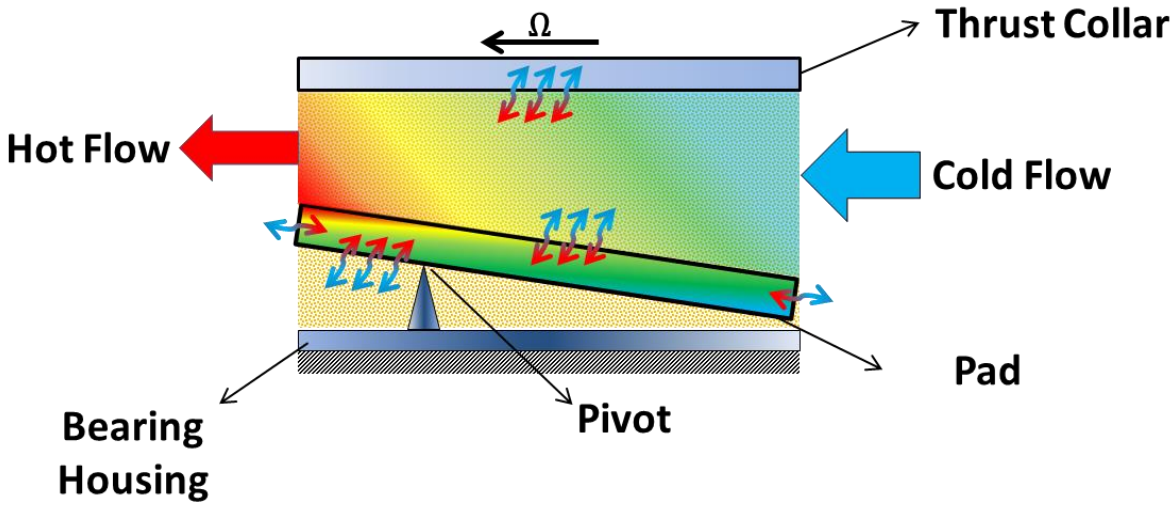

Figure 3. Schematic view of boundary conditions for the fluid film and a pad.

At a steady state condition, Jeng et al. [5] state the thermal energy transport equation of an incompressible fluid with temperature $T_{(r,\theta,z)}$, as

$$\rho c_P\left[U\frac{\partial T}{\partial r}+V\frac{\partial T}{r\partial\theta}+W\frac{\partial T}{\partial z}\right]=\kappa\left[\frac{1}{r}\frac{\partial}{\partial r}\left(r\frac{\partial T}{\partial r}\right)+\frac{1}{r^2}\frac{\partial T^2}{\partial\theta^2}+\frac{\partial T^2}{\partial z^2}\right]$$
$$+\mu\left(1+\frac{\epsilon_m}{\nu}\right)\left[\left(\frac{\partial U}{\partial z}\right)^2+\left(\frac{\partial V}{\partial z}\right)^2\right] \quad (11)$$

where ρ, c_p, and κ are the lubricant density, specific heat, and conductivity, respectively. These parameters are assumed constant over the flow domain. Fluid velocity components are calculated through Eqns. (8) to (10). $\frac{\epsilon_m}{\nu}$ is the ratio of eddy viscosity (ϵ_m) over dynamic viscosity (ν) and is a function of flow turbulence (See Appendix A). The fluid viscosity (μ) is a function of local temperature (T),

$$\mu=\mu_*\, e^{-\alpha_{VT}(T-T_*)} \quad (12)$$

where μ_* and T_* are fluid viscosity and temperature at supply condition. α_{VT} is a fluid temperature-viscosity coefficient. The solution of energy equation requires boundary conditions,

i. At the pad leading edge $(\theta=\theta_l,\ R_{in}<r<R_{out},\ e_c-h<z<e_c),\ T=T_l$ (13.a)

ii. At the thrust collar surface $(\theta_l<\theta<\theta_t,\ \ R_{in}<r<R_{out}, z=e_c-h),\ \ T=T_l$ (13.b)

iii. At the pad surface $(\theta_l<\theta<\theta_t,\ \ R_{in}<r<R_{out}, z=e_c)$

$$q_{\text{film}\rightarrow\text{pad}}=-\kappa\frac{\partial T}{\partial z}=q_{\text{into pad}}=-\kappa_p\frac{\partial T_p}{\partial z} \quad (13.c)$$

where Eqn. (13.c) governs the flow of heat from the fluid film to the pad surface and conducted internally. T_p is the pad temperature, (R_{in}, R_{out}) are the inner radius and outer radius of a pad, and (θ_l , θ_t) are the circumferential location of the leading edge and the trailing edge, respectively.

Figure 4 shows the lubricant supplied into the bearing at a known supply temperature (T_*) that mixes with the hot lubricant leaving the upstream pad with temperature T_e and flow rate Q_e. A conventional thermal mixing model at a bearing feeding port determines the downstream pad leading edge temperature (T_l) and flow rate (Q_l) from the upstream pad trailing edge flow (Q_e,

T_e) and the (cold) supply flow (Q_*, T_*). That is

$$Q_* = Q_l - \lambda_{mix} Q_e \tag{14.a}$$

$$Q_l\, T_l = Q_*\, T_* + \lambda_{mix} Q_e T \tag{14.b}$$

where λ_{mix} is a lubricant thermal mixing coefficient, an empirical parameter that depends on the lubrication feed arrangement.

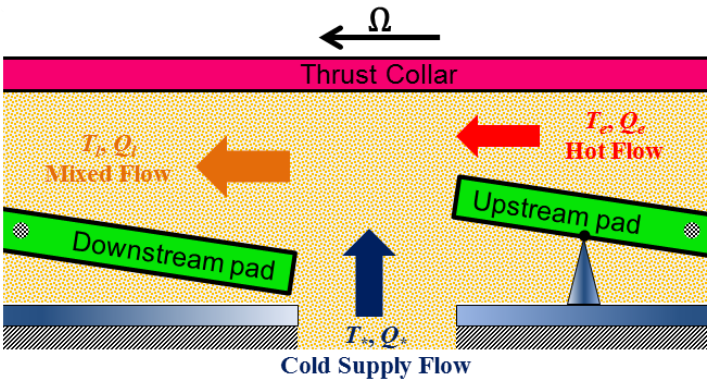

Figure 4: Mixing of hot oil from the upstream pad with cold supply flow in a feed groove region.

2.3 The Heat Conduction Equation in a Pad

The steady-state heat conduction equation governing the flow of heat through a pad with isotropic conductivity is [3]

$$\nabla^2 T_P = \frac{1}{r}\frac{\partial}{\partial r}\left(r\frac{\partial T_P}{\partial r}\right) + \frac{1}{r^2}\frac{\partial^2 T_P}{\partial \theta^2} + \frac{\partial^2 T_P}{\partial z^2} = 0 \tag{15}$$

The top surface of a pad is in contact with the fluid film and experiences a heat flux condition governed by Equation (10.c). For the back surface and side surfaces, the boundary condition consistent with the physics of the problem is [3]

$$q_{\text{pad}\rightarrow\text{environment}} = -\kappa_p \frac{\partial T_p}{\partial n} = \lambda\left(T_p - T_*\right) \tag{16}$$

and states that the heat flux at the surface is carried away through the convection. κ_p is a pad conductivity coefficient and λ is a fluid flow heat convection coefficient. The $\frac{\partial}{\partial \mathrm{n}}$ is the derivative along the normal direction to the pad surface.

2.4 Perturbation Analysis

At the equilibrium position, a small amplitude motion of a thrust collar (Δe_c) with frequency ω is followed by pad motions (Δe_P, $\Delta\alpha, \Delta\beta$) with similar frequency. Hence, ($i = \sqrt{-1}$),

$$\begin{aligned} e_c &= e_{c0} + \Delta e_c \; e^{i\omega t} \\ e_P &= e_{P0} + \Delta e_P \; e^{i\omega t} \\ \alpha &= \alpha_0 + \Delta\alpha \; e^{i\omega t} \\ \beta &= \beta_0 + \Delta\beta \; e^{i\omega t} \end{aligned} \tag{17}$$

See Figure 5 for a schematic view of a pad and thrust collar motions from equilibrium position.

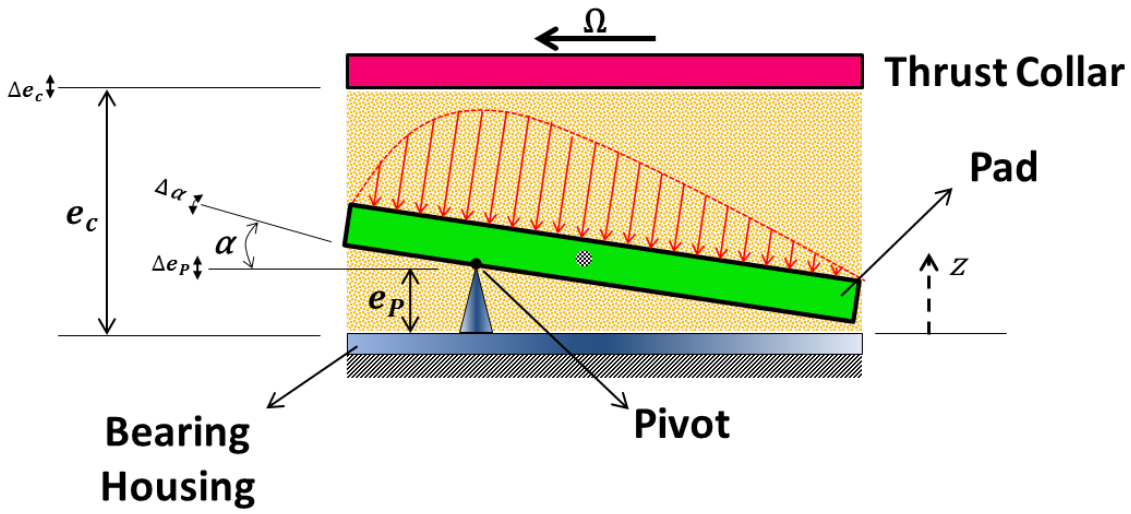

Figure 5. Schematic view of thrust collar motion (Δe_c) from an equilibrium position.

The fluid film thickness and the hydrodynamic pressure field are the superposition of an equilibrium field (zeroth order) and perturbed fields (first order),

$$h_{(r,\theta,t)} = h_0 + \left(\sum h_X \; \Delta X\right) e^{i\omega t} \tag{18}$$

$$P_{(r,\theta,t)} = P_0 + \left(\sum P_X \; \Delta X\right) e^{i\omega t} \tag{19}$$

where the index X= e_c, e_P, α, and β; and

$$
\begin{aligned}
h_{e_c} &= 1 \\
h_{e_P} &= -1 \\
h_\alpha &= r\sin\left(\theta_P - \theta\right) \\
h_\beta &= r\cos\left(\theta_P - \theta\right) - R_P
\end{aligned}
\tag{20}
$$

Substituting Eqns. (18) and (19) into Reynolds equation (Eqn.(2)) leads to partial differential equations (PDEs) for the static pressure field (P_0) and the perturbation pressure fields (P_{e_c}, P_{e_P}, P_α, and P_β). Let, $L(O)$ represents the differential operator,

$$
L(O) = \frac{1}{r}\frac{\partial}{\partial r}\left(H_{r_0} r \frac{\partial O}{\partial r}\right) + \frac{1}{r}\frac{\partial}{\partial \theta}\left(H_{\theta_0}\frac{1}{r}\frac{\partial O}{\partial \theta}\right) \tag{21}
$$

Then, the PDE equation for the static pressure field (zeroth order) is

$$
L(P_0) = \Omega\frac{\partial G_0}{\partial \theta} \tag{22}
$$

and the PDEs for the first order pressure fields are

$$
L\left(P_{e_c}\right) = -\frac{1}{r}\frac{\partial}{\partial r}\left(r\frac{\partial H_r}{\partial h}\frac{\partial P_0}{\partial r}\right) - \frac{1}{r}\frac{\partial}{\partial \theta}\left(\frac{1}{r}\frac{\partial H_\theta}{\partial h}\frac{\partial P_0}{\partial \theta}\right) + i\,\omega \tag{23.a}
$$

$$
L\left(P_{e_P}\right) = -L\left(P_{e_c}\right) \tag{23.b}
$$

$$
L\left(P_\alpha\right) = \Omega\frac{\partial G}{\partial h}\frac{\partial h_\alpha}{\partial \theta} - \frac{1}{r}\frac{\partial}{\partial r}\left(r\frac{\partial H_r}{\partial h}\frac{\partial P_0}{\partial r}\,h_\alpha\right) - \frac{1}{r}\frac{\partial}{\partial \theta}\left(\frac{1}{r}\frac{\partial H_\theta}{\partial h}\frac{\partial P_0}{\partial \theta}\,h_\alpha\right) + i\omega\,h_\alpha \tag{23.c}
$$

$$
L\left(P_\beta\right) = \Omega\frac{\partial G}{\partial h}\frac{\partial h_\beta}{\partial \theta} - \frac{1}{r}\frac{\partial}{\partial r}\left(r\frac{\partial H_r}{\partial h}\frac{\partial P_0}{\partial r}\,h_\beta\right) - \frac{1}{r}\frac{\partial}{\partial \theta}\left(\frac{1}{r}\frac{\partial H_\theta}{\partial h}\frac{\partial P_0}{\partial \theta}\,h_\beta\right) + i\omega\,h_\beta \tag{23.d}
$$

See Eqn. (20) for h_α and h_β. Here,

$$
\frac{\partial H_r}{\partial h} = \frac{\xi_4(h)\int_0^h \xi_3(\hat{z})\,d\hat{z} - \xi_3(h)\int_0^h \xi_4(\hat{z})\,d\hat{z}}{\left(\int_0^h \xi_4(\hat{z})\,d\hat{z}\right)^2}\int_0^h\left(\int_0^{\hat{z}}\xi_4(\delta)\,d\delta\right)d\hat{z} \tag{24}
$$

$$
\frac{\partial H_\theta}{\partial h} = \frac{\xi_2(h)\int_0^h \xi_1(\hat{z})\,d\hat{z} - \xi_1(h)\int_0^h \xi_2(\hat{z})\,d\hat{z}}{\left(\int_0^h \xi_2(\hat{z})\,d\hat{z}\right)^2}\int_0^h\left(\int_0^{\hat{z}}\xi_2(\delta)\,d\delta\right)d\hat{z} \tag{25}
$$

$$\frac{\partial G}{\partial h}=\frac{\xi_4(h)}{\left(\int_0^h \xi_4(\hat{z})\,d\hat{z}\right)^2}\int_0^h\left(\int_0^{\hat{z}}\xi_4(\delta)\,d\delta\right)d\hat{z} \tag{26}$$

In a laminar flow with a constant viscosity cross the fluid film,

$$\frac{\partial H_r}{\partial h}=\frac{\partial H_\theta}{\partial h}=\frac{3h^2}{12\mu},\ \ \frac{\partial G}{\partial h}=\frac{1}{2} \tag{27}$$

2.5 Fluid Film Forces and Moments

Let F_{η_0} and (M_{γ_0}, M_{ξ_0}) represent the force and moments induced by the static pressure (fluid film static force and moments) acting on a pad

$$F_{\eta_0}=-\int_{R_{in}}^{R_{out}}\int_{\theta_l}^{\theta_t}P_0\ r\ dr\ d\theta \tag{28}$$

$$M_{\gamma_0}=\int_{R_{in}}^{R_{out}}\int_{\theta_l}^{\theta_t}\left[P_0\left(r\sin\left(\theta-\theta_p\right)\right)\ r\ dr\ d\theta\right] \tag{29}$$

$$M_{\xi_0}=\int_{R_{in}}^{R_{out}}\int_{\theta_l}^{\theta_t}\left[P_0\left(r\cos\left(\theta-\theta_p\right)-R_p\right)\ r\ dr\ d\theta\right] \tag{30}$$

At the equilibrium condition, the fluid film static moments over each pad, M_{γ_0} and M_{ξ_0}, are balanced against the static pivot reaction moments, $M_{\gamma_{P_0}}$ and $M_{\xi_{P0}}$. If the structural pivot reaction moments are zero (pad is free to tilt, $M_{\gamma_{P_0}}=M_{\xi_{P0}}$ =0), a pad tilts into a position where the fluid film static moments are also zero. Appendix B details a model for pivot structural stiffness coefficients. The combination of the static force (sum of all pads) acting on the thrust collar balances the applied force.

The complex dynamic stiffness coefficient matrix, consisting of real and imaginary parts, are calculated using the perturbation pressure fields,

$$Z_{XY}=K_{XY}+i\omega\ C_{XY}=-\int_{R_{in}}^{R_{out}}\int_{\theta_l}^{\theta_t}\left(P_Y\right)\ L_X\ r\ dr\ d\theta \tag{31}$$

where $Y=e_c,e_P,\alpha,\beta$, $X=z,\eta,\gamma,\xi$ and

$$
\begin{aligned}
L_z &= 1 \\
L_\eta &= -1 \\
L_\gamma &= \left[r \sin\left(\theta_P - \theta\right) \right] \\
L_\xi &= \left[r \cos\left(\theta_P - \theta\right) - R_P \right]
\end{aligned}
\tag{32}
$$

The complex stiffness coefficients for pad axial motions and the thrust collar axial motions are equal in magnitude but opposite in sign,

$$
Z_{ze_c} = -Z_{ze_P} \tag{33}
$$

2.6 Frequency Reduced Model

Considering a pad as a rigid body (disregarding structure flexibility), its equation of motion is,

$$
\mathbf{M} \begin{bmatrix} \ddot{e}_P \\ \ddot{\alpha} \\ \ddot{\beta} \end{bmatrix} = \begin{bmatrix} F_\eta \\ M_\gamma \\ M_\xi \end{bmatrix} + \begin{bmatrix} F_{\eta_p} \\ M_{\gamma_p} \\ M_{\xi_p} \end{bmatrix} \tag{34}
$$

where F_{η_p}, M_{γ_p} and M_{ξ_p} are respectively a pivot reaction force and the reaction moments. The pad mass matrix ($\mathbf{M}$) is,

$$
\mathbf{M} = \begin{bmatrix} m & m\xi_G & m\gamma_G \\ m\xi_G & I_\gamma + m{\xi_G}^2 & 0 \\ m\gamma_G & 0 & I_\xi + m{\gamma_G}^2 \end{bmatrix} \tag{35}
$$

here, m is the mass of a pad and ($I\gamma, I_\xi$) are its mass moment of inertia with respect to the (γ, ξ) axes. The mass center of a pad (G) is located at $(\gamma_G, \xi_G, \eta_G)$, see Figure 2.

In Eqn. (34), the fluid film force and moments as well as the pivot reaction force and moments consist of static and dynamic parts, hereby written as,

$$
\begin{bmatrix} F_\eta \\ M_\gamma \\ M_\xi \end{bmatrix} = \begin{bmatrix} F_{\eta_0} \\ M_{\gamma_0} \\ M_{\xi_0} \end{bmatrix} - \mathbf{Z}_C \Delta e_c \, e^{i\omega t} - \mathbf{Z}_P \begin{Bmatrix} \Delta e_P \\ \Delta\alpha \\ \Delta\beta \end{Bmatrix} e^{i\omega t} \tag{36}
$$

$$\begin{bmatrix} F_{\eta_p} \\ M_{\gamma_p} \\ M_{\xi_p} \end{bmatrix} = \begin{bmatrix} F_{\eta_{p0}} \\ M_{\gamma_{p0}} \\ M_{\xi_{p0}} \end{bmatrix} - \mathbf{Z}_{P_S} \begin{Bmatrix} \Delta e_P \\ \Delta\alpha \\ \Delta\beta \end{Bmatrix} e^{i\omega t} \tag{37}$$

where,

$$\mathbf{Z}_C = \begin{bmatrix} Z_{\eta e_c} \\ Z_{\gamma e_c} \\ Z_{\xi e_c} \end{bmatrix}, \qquad \mathbf{Z}_P = \begin{bmatrix} Z_{\eta e_P} & Z_{\eta\alpha} & Z_{\eta\beta} \\ Z_{\gamma e_P} & Z_{\gamma\alpha} & Z_{\gamma\beta} \\ Z_{\xi e_P} & Z_{\xi\alpha} & Z_{\xi\beta} \end{bmatrix}, \qquad \mathbf{Z}_{P_S} = \begin{bmatrix} Z_{\eta e_{PS}} & Z_{\eta\alpha_S} & Z_{\eta\beta_S} \\ Z_{\gamma e_{PS}} & Z_{\gamma\alpha_S} & Z_{\gamma\beta_S} \\ Z_{\xi e_{PS}} & Z_{\xi\alpha_S} & Z_{\xi\beta_S} \end{bmatrix} \tag{38}$$

here, Z_{XY}(X=z, ɣ, ξ and Y =e_c, e_P, α, β) are a pad complex dynamic stiffness coefficients defined as $Z_{XY} = K_{XY} + i\omega C_{XY}$. Appendix B details a model for pivot structural complex stiffness. Substitution of Eqns. (36) and (37) into Eqn. (34) gives,

$$\left(\mathbf{Z}_{P_S} - \omega^2\mathbf{M} + \mathbf{Z}_P\right) \begin{Bmatrix} \Delta e_P \\ \Delta\alpha \\ \Delta\beta \end{Bmatrix} = -\mathbf{Z}_C \, \Delta e_c \tag{39}$$

Note that, the pivot static reaction force and moments are in balance with the fluid film static force and moments on the pad, i.e.,

$$\begin{bmatrix} F_{\eta_0} \\ M_{\gamma_0} \\ M_{\xi_0} \end{bmatrix} + \begin{bmatrix} F_{\eta_{p0}} \\ M_{\gamma_{P0}} \\ M_{\xi_{P0}} \end{bmatrix} = \begin{bmatrix} 0 \\ 0 \\ 0 \end{bmatrix} \tag{40}$$

The hydrodynamic force acting on the thrust collar against the axial load also consists of static and dynamic parts,

$$F_z = F_{z_0} - Z_{zz}\,\Delta e_c e^{i\omega t} - \mathbf{Z}_z \begin{Bmatrix} \Delta e_P \\ \Delta\alpha \\ \Delta\beta \end{Bmatrix} e^{i\omega t} \tag{41}$$

where, $\mathbf{Z}_z = \begin{bmatrix} Z_{ze_P} & Z_{z\alpha} & Z_{z\beta} \end{bmatrix}$.

Then, substitution of Eqn. (39) into (41) results in an equation for the axial force F_z as a function of the static force and the thrust collar axial displacement (Δe_c).

$$F_z = F_{z_0} - \left(Z_{zz} - \mathbf{Z}_z \left(\mathbf{Z}_{P_S} - \omega^2 \mathbf{M} + \mathbf{Z}_P \right)^{-1} \mathbf{Z}_C \right) \Delta e_c \, e^{i\omega t} \tag{42}$$

Therefore, for a bearing with N_p number of pads, the components of the axial stiffness K_R and axial damping C_R (frequency reduced) are

$$Z_R = K_R + i\omega C_R = N_p \left(Z_{zz} - \mathbf{Z}_z \left(\mathbf{Z}_{P_S} - \omega^2 \mathbf{M} + \mathbf{Z}_P \right)^{-1} \mathbf{Z}_C \right) \tag{43}$$

3. COMPARISON OF PREDICTIONS AGAINST TEST DATA

The measurements in Refs. [3,4] are compared against predictions obtained by the current THD model. Table 2 outlines the geometry, lubricant properties, operating condition, and thermal properties of a test TPTB.

Table 2. Characteristics of a TPTB tested by Almqvist et al. [3] and Glavatskih [4]

Bearing Properties	
Number of pads (N_p)	6
Outer radius (R_{out})	114.3 [mm]
Inner radius (R_{in})	57.15 [mm]
Arc	50 [°]
Pad thickness (t_p)	28.58 [mm]
Pivot radial offset	50%
Pivot circumferential offset	60%
Pad mass (m)[1]	0.1 kg
Pad moment of inertia around γ-axis (I_γ)[1]	0.01 kg.m^2
Pad moment of inertia around ξ-axis (I_ξ)[1]	0.008 kg.m^2
Pad mass radial offset (γ_G)[1]	-0.05 m
Pad mass circumferential offset (ξ_G)[1]	-0.08 m
Pivot axial stiffness coefficients ($K_{\eta e_{PS}}$)[1]	5×10^8 N/m
Pivot axial damping ($C_{\eta e_{PS}}$)[1]	0
Fluid Properties	
Lubricant	ISO VG46
Viscosity at supply temperature (μ_*)	39 [mPa.s]
Viscosity-Temperature coefficient[1] (α_{VT})	0.0345 [1/˚C]
Density (ρ)	820 [kg/m^3]
Specific heat capacity (c_p)	2190 [J/(kg ˚C)]
Thermal conductivity coefficient (K)	0.15 [W/(m ˚C)]
Heat transfer coefficient (λ)	500 [W/(m^2 ˚C]
Operating Condition	
Load (W_z)	0.5-2.0 [MPa]
Rotor speed (N)	1.5-3 [krpm]
Supply pressure[1] (P_*)	0 [bar]
Ambient pressure$_1$ (P_a)	0 [bar]
Supply temperature (T_*)	30-60 [°C]
Thermal Properties	
Conductivity coefficient of Pads (κ_P)	51 [W/(m ˚C)]
Thermal mixing coefficient in grooves (λ_{mix})[1]	0.8

[1] Assumed or calculated based on the available data in Ref. [3]

Figure 6 shows cross section views of the test rig used by Almqvist et al. [3] and Glavatskih [4]. Hydraulic cylinders ⑧ and ⑨, located between bearing holders, apply a load on the test TPTB ①. The test rig includes a lubricant supply system consisting of an oil reservoir, a screw pump, a filter, and a heat exchanger.

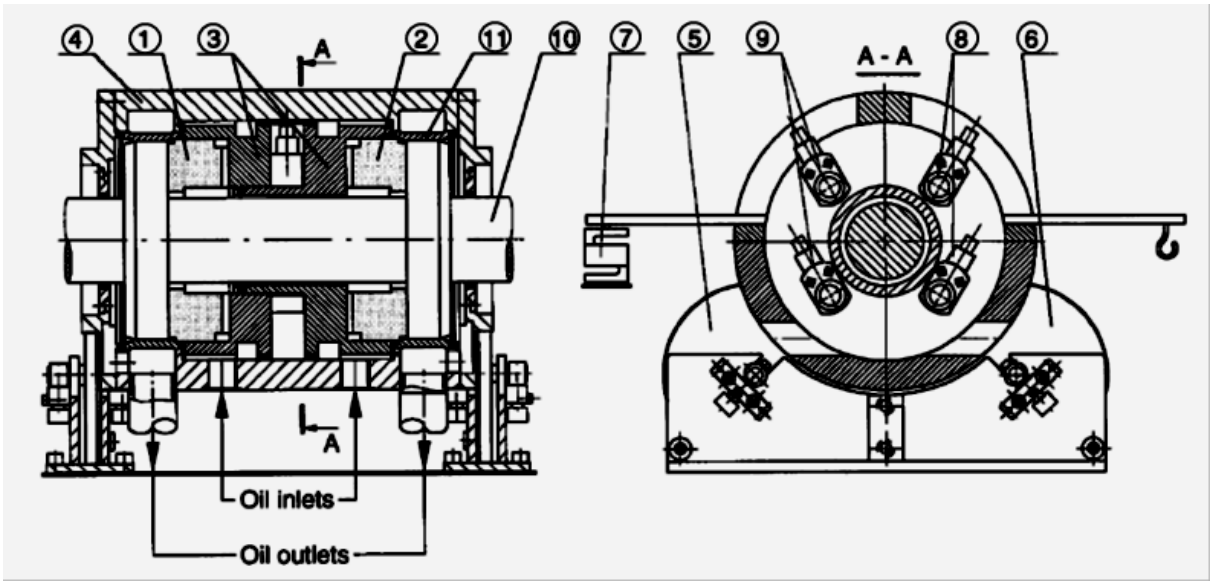

Figure 6. Section views of a test rig used in [3,4] to evaluate the performance of a TPTB.

The housing is free to turn (mounted on four rolling elements), but a strain sensor ⑦ prevents it from rotation. The force, measured using strain sensor ⑦, is induced by the friction torque acting on the bearing housing and leads to the calculation of the drag power loss in the bearing. A 143 kW DC motor, with a maximum speed of 1.8 krpm, drives the test rig. Higher rotor speeds can be reached by using pulley sections.

Figure 7 demonstrates the arrangement of the sensors mounted on a test TPTB ①. The thrust collar is shown partially for clarity. Two pressure transducers, P_c 25 and P_c 75, mounted on the thrust collar, rotate with it and measure the pressure at the locations of 25% and 75% of pad radial length. The distance sensors H_l and H_t are located at the center leading edge and the trailing edge of pad ⑤, respectively. Thermocouples T_{p3} 75/75 and T_{p6} 75/75 are placed 3mm under the top surface of pads ③ and ⑥ at the location of 75/75[1].

[1] Location 75/75 indicates a point on a pad which is 75% of the pad circumferential length away from the pad leading edge and 75% of the pad radial length away from the pad inner radius.

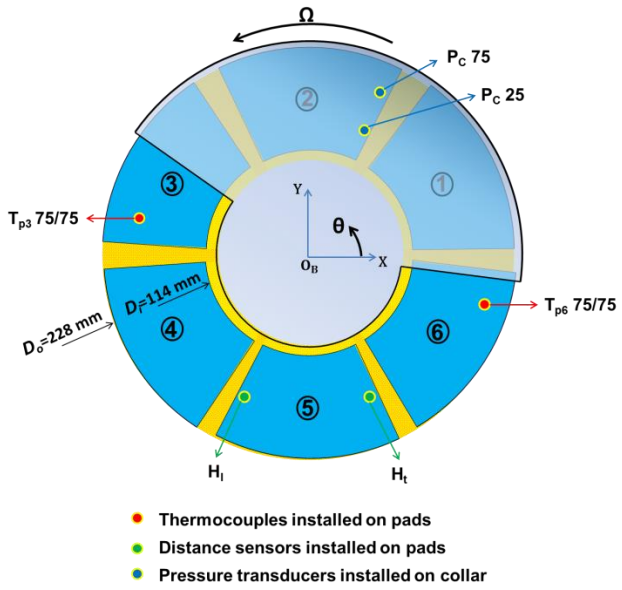

Figure 7. Location of instruments on a test TPTB used in Refs. [3,4] (thrust collar is shown partially).

Table 3 lists the uncertainties of the measurements report in Ref. [3]. The works of Almqvist et al and Glavatskih have low measurement uncertainties which make them reliable resources to evaluate the predictions made by the model.

Table 3. Measurement uncertainities in Ref. [3]

Parameter	value
Pad sub-surface temperature	±1 K
Fluid film pressure	±4 % of measured magnitude
Fluid film thickness	±1.5 μm
Power loss	±1 % of measured magnitude

The authors obtain data for distinct applied load, rotor speed, and lubricant supply temperature. The following figures show the predictions made by the current THD model versus the test data obtained for hydrodynamic pressure, pad subsurface temperature, fluid film thickness, and shear drag power loss.

3.1 Predictions of Hydrodynamic Pressure Field

Figure 8 shows predictions and test data for the hydrodynamic pressure field on pad ④ at the radial locations of 25% and 75%. Ref.[3] measures the pressure using two pressure transducers

on the thrust collar (see Figure 7 for the locations of the pressure transducers). The operating condition consists of rotor speed at 1.8 krpm, a specific load of 1.5 MPa, and oil supplied with a temperature of 50 ˚C. The predictions made by the current THD model show a very good agreement with test data with a maximum difference of 8%[1]. Observe that the maximum difference occurs at the peak pressure spot and the pressure is over-predicted. A possible source of error could be neglecting of pad deformations induced by both pressure and temperature changes.

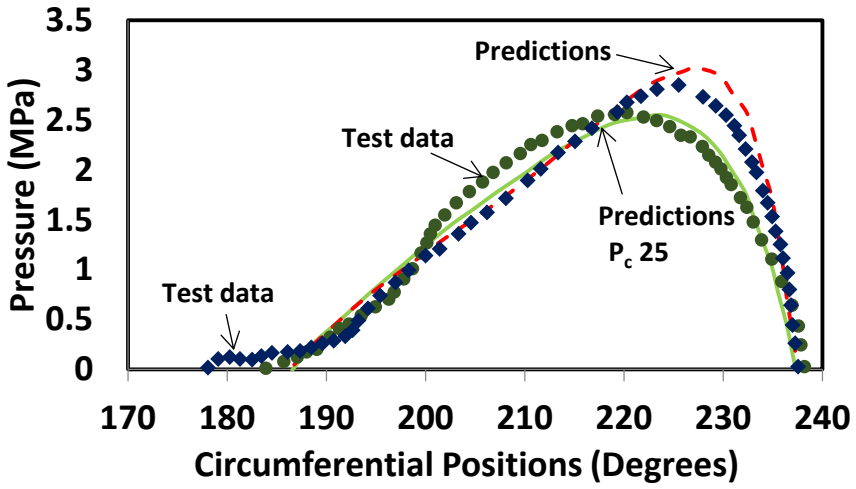

Figure 8. Predictions and test data for hydrodynamic pressure. Measured data from [3]. (Operating under a specific load of 1.5 MPa, with a rotor speed of 1.8 krpm, and with oil supply temperature at 50 ˚C)

3.2 Predictions of Temperature Distribution in a Pad

Figure 9 depicts predictions and test data (from Ref. [4]) for the temperature rise relative to supply temperature(40 ˚C), in a point located 3 mm under the pad top surface at the location of 75/75 (see Figure 7 for the locations of thermocouples). On the left, the temperature rise is shown versus specific load (ranging from 0.5 to 2.0 MPa) for rotor speed equal to 1.5 and 3 krpm. On the right, temperature rise for specific load equal to 1.0 and 2.0 MPa is shown versus rotor speed (from 1.5 to 3 krpm). There is a good agreement between predictions and test data with a maximum difference is 9%, the predicted temperature rise is 2.2 ˚C less than the test data. The difference between predictions and test data mainly increases with an increase in either load

[1] The percentage of error is calculated by dividing the difference over the test data.

or speed.

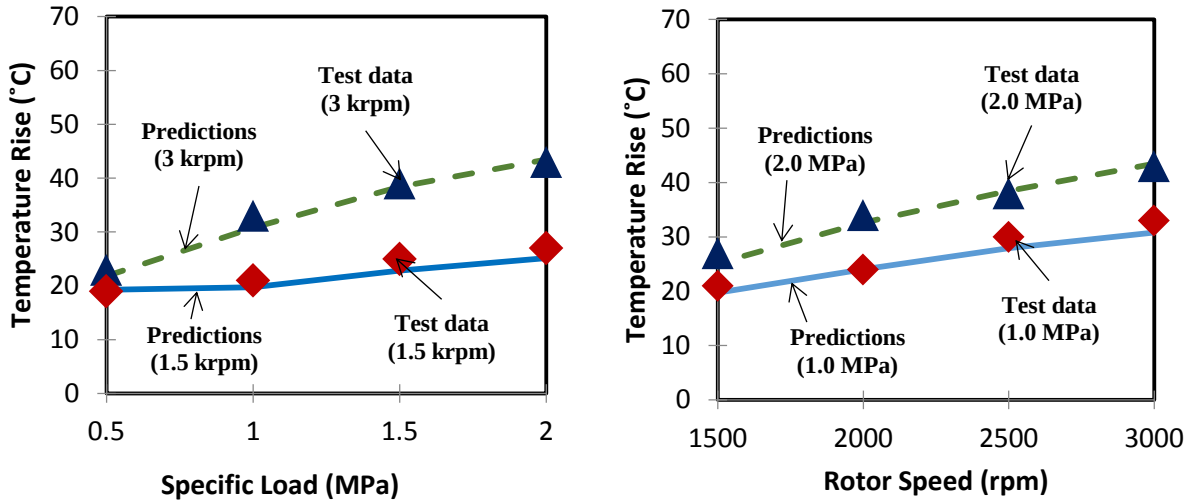

Figure 9. Predictions and test data for pad subsurface temperature rise at the location 75/75, left: versus specific load, and right: versus rotor speed. Measured data from Ref. [4]. (Oil supply temperature at 40 °C)

Figure 10 shows predictions and test data for pad subsurface temperature rise at the location 75/75, for oil supply temperature equal to 30 ˚C and 60 ˚C versus specific load (left) and versus rotor speed (right). Predictions match measurements with a maximum difference of 17%, the predicted temperature rise is 6 °C less than the measured magnitude. Observe that predictions and test data differ more at the lowest supply temperature.

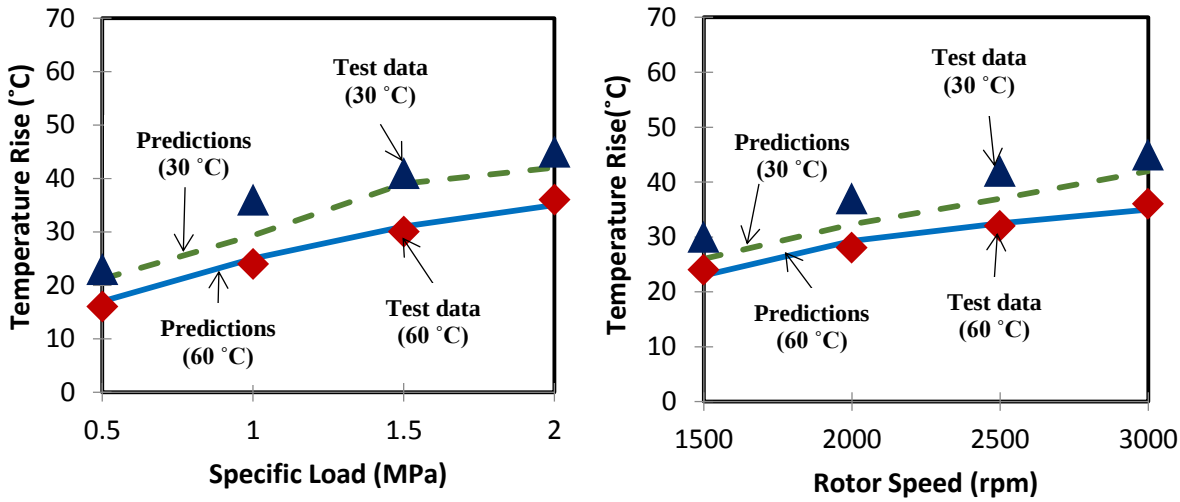

Figure 10. Predictions and test data for pad subsurface temperature rise at the 75/75 location for oil supply temperature equal to 30 ˚C and 60 ˚C, left: versus specific load (with a rotor speed of 3 krpm), and right: versus rotor speed (under a specific load of 2.0 MPa). Measured data from Ref. [4].

3.3 Predictions of Film Thickness

Figure 11 benchmarks the predicted fluid film thickness on pad ⑤ against test data in Ref. [4]. On the left, the fluid film thickness at the center of the leading edge is shown versus specific loads, for rotor speed equal to 1.5 and 3 krpm. On the right, fluid film thickness at the center of the trailing edge is depicted versus rotor speed, under specific load equal to 1.0 and 2.0 MPa. See Figure 7 for the location of distance sensors on pad ⑤. Supply lubricant temperature is at 40 °C. Predictions made by the current model are in agreement with test data with a maximum difference of 20%, at the maximum load of 2.0 MPa.

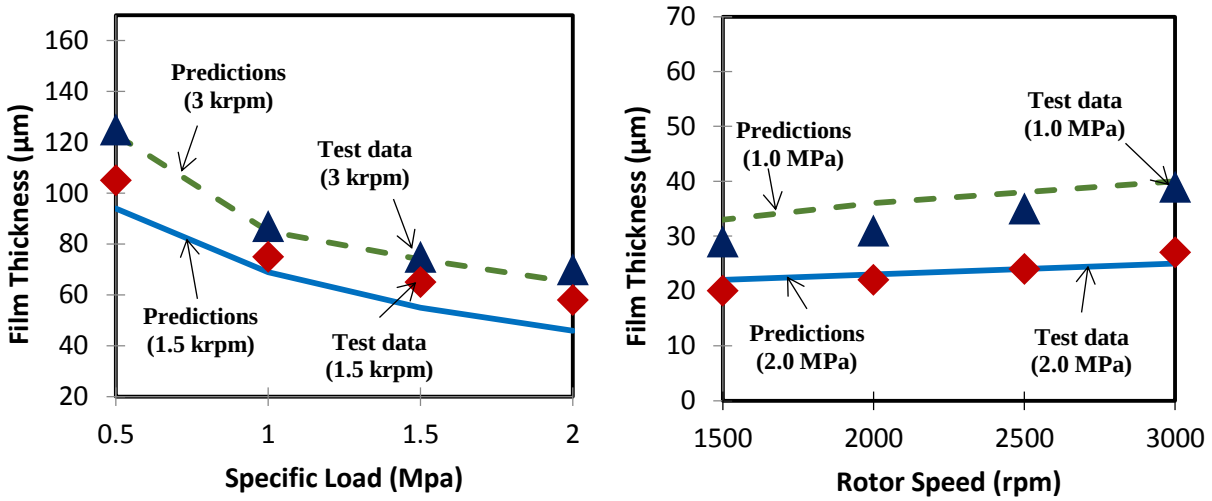

Figure 11. Predictions and test data for the fluid film thickness, left: at the center of leading edge versus specific load, right: at the center of trailing edge versus rotor speed. Measured data from Ref. [4]. (Oil supply temperature at 40 °C)

Figure 12 shows the predicted and measured fluid film thickness on pad ⑤ for oil supply temperature equal to 30 ˚C and 60 ˚C. On the right, the fluid film thickness at the center of the leading edge (top) and the trailing edge (bottom) are shown versus specific load (rotor speed of 3 krpm). On the left, the fluid film thickness at the center of the leading edge and the trailing edge are depicted versus rotor speed (specific load at 2.0 MPa). Predictions match the test data from Ref. [4], with a maximum difference of 13.3%. Observe that the difference increases at the lowest oil supply temperature (bottom left in Figure 12). Also note that the fluid film thickness increases if the supply temperature decreases. This is due to larger fluid viscosity.

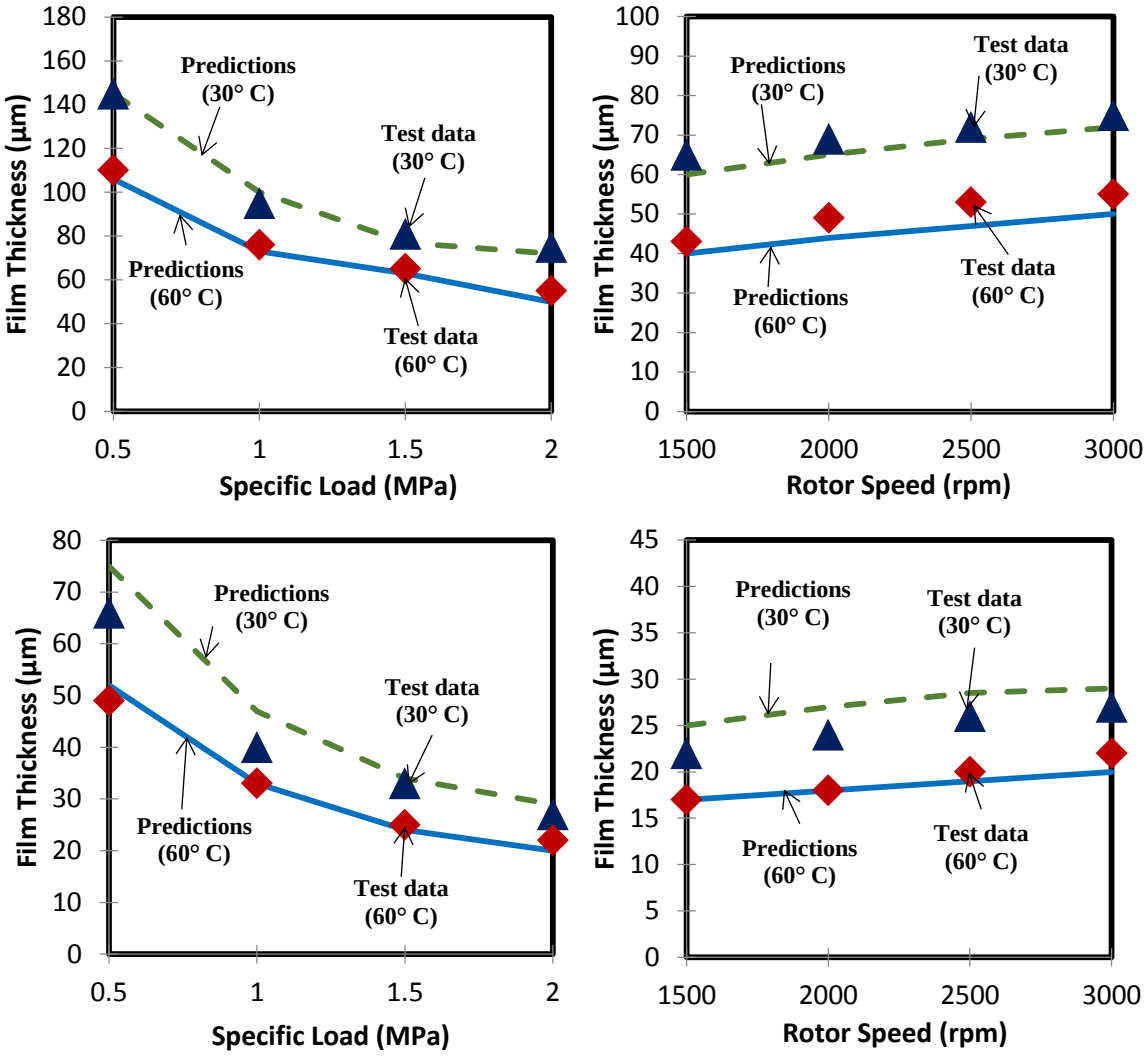

Figure 12. Predictions and test data for the fluid film thickness with oil supply temperature equal to 30 ˚C and 60 ˚C, top left: at the center of leading edge versus specific load, top right: at the center of leading edge versus rotor speed, bottom left: at the center of trailing edge versus specific load, and bottom right: at the center of trailing edge versus rotor speed. Measured data from Ref. [4]. (Left: with a rotor speed of 3 krpm, right: under a specific load of 2.0 MPa)

3.4 Predictions of Drag Power Loss

Figure 12 shows the predicted and measured shear drag power loss versus specific load operating with speed equal to 1.5 and 3 krpm (left); and versus rotor speed under specific load of 1.0 and 2.0 MPa (right). The oil supply temperature is at 40 °C. Predictions are in an agreement with the test data from Ref. [4]. A maximum difference of 6 % occurs at the top speed of 3 krpm

and under a load of 2.0 MPa.

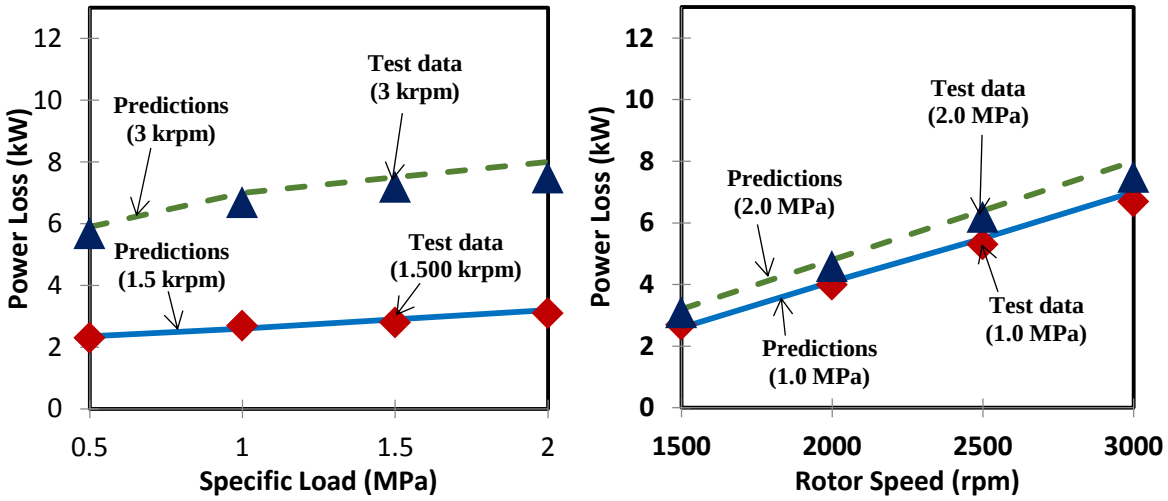

Figure 13. Predictions and test data for power loss, left: versus specific load, and right: versus rotor speed. Measured data from Ref. [4]. (Oil supply temperature at 40 °C)

Figure 14 depicts the predictions and test data for power loss operations with oil supply temperature (T_*) at 30 ˚C and 60 ˚C. Likewise, on the left, power loss is shown versus specific load with a rotor speed of 3 krpm and, on the right, versus rotor speed under a specific load of 2.0 MPa. Predictions match the test data with a maximum difference of 8% at the lowest supply temperature (30 °C). Observe that the difference mainly increases as either speed or load increases.

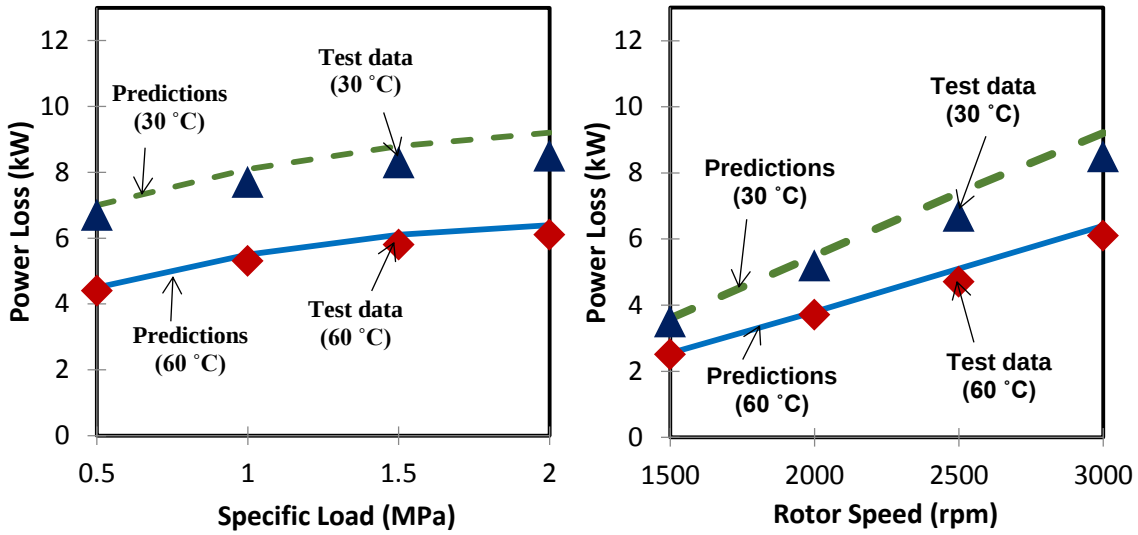

Figure 14. Predictions and test data for power loss for oil supply temperature equal to 30 ˚C and 60 ˚C, left: versus specific load (with a rotor speed of 3 krpm), and right: versus rotor speed (under a specific load of 2.0 MPa). Measured data from Ref. [4].

CONCLUSION AND PROPOSED FUTURE WORK

This report detailed a thermo-hydrodynamic (THD) analysis for the performance predictions of tilting pad thrust bearings (TPTBs). The model simulates the operating of a TPTB and predicts static forced performance characteristics and axial force coefficients to better design TPTBs. The analysis process is fast enough to assure efficiency with accuracy.

A generalized Reynolds equation, accounting for cross-film viscosity variation and turbulent flow effects, gives a 2D pressure field, then, a thermal energy transport equation in the fluid film couples to a 3D heat conduction equation in a pad and predicts temperature distribution. A perturbation analysis calculates dynamic force coefficients for pad motions and thrust collar axial motions. A pad has three DOFs, two rotational modes (tilting) and one axial displacement. Dynamic force coefficients conjugate with a pivot stiffness model to deliver frequency reduced axial stiffness and damping coefficients for the bearing.

The model assumes identical fluid film thickness for all pads (disregarding the thrust collar misalignments).Operating with identical fluid film thickness leads to equal predictions for all pads. Hence, this report detailed analysis only for one pad in a turbulent flow TPTB. To calculate the force coefficients of a bearing ([K,C]), predictions for a single pad are multiplied by the number of pads (N_P).

To check the accuracy of the model, predictions from the current THD model are compared against archival test data [3,4] for a six-pad TPTB with 228 mm in diameter operating under specific load ranging from 0.5 to 2.0 MPa, rotor speed between 1.5 and 3 krpm (mean surface speed of ΩR_m=14-28 m/s). The operating conditions include oil supply temperature at 30, 40 , and 60 ˚C. Predictions show a good agreement with test data with differences up to 9% for pressure field, 17% for pad subsurface temperature rise, 20% for fluid film thickness, and 8% for drag power loss.

Predictions by the current THD model are accurate for a medium size TPTB (228 mm OD) [3,4]. Differences between predictions and measurements generally increase as the load or shaft speed increases. The literature review describes the need for more complex models, e.g. TEHD models, to accurately predict performance of a TPTB for high power density conditions. To extend the current model into a TEHD model, pad deformations due to pressure and temperature

changes should be included. In addition, in a TPTB, thrust collar misalignments largely change the operating fluid film thickness. Accounting for thrust collar tilt motions in the model is important to increase the accuracy in static load performance predictions, and also to quantify the reaction moments and moment/tilt coefficients.

REFERENCES

[1] San Andrés, L., and Zirkelback, N., 1996, "Simplified Analysis of Hydrodynamic Thrust Bearing, " Research Progross Report to the TAMU Turbomachinary Research Consorsium, TRC-B&C-4-96, Texas A&M University.

[2] Wood, H., 2015, "Rotating Machinery & Controls, " Fall Romac Newsletter To Romac Industrial Memebers, University of Virginia.

[3] Almqvist, T., Glavatskih, S. B., and Larsson, R., 1999, "THD Analysis of Tilting Pad Thrust Bearings - Comparison Between Theory and Experiments, " J. Tribol., **122**(2), pp. 412–417.

[4] Glavatskikh, S. B., 2001, "Steady State Performance Characteristics of a Tilting Pad Thrust Bearing," J. Tribol., **123**(3), pp. 608–215.

[5] Jeng, M. C., Zhou, G. R., and Szeri, A. Z., 1986, "A Thermohydrodynamic Solution of Pivoted Thrust Pads : Part I — Theory," J. Tribol., **108**, pp. 195–207.

[6] Jeng, M. C., Zhou, G. R., and Szeri, A. Z., 1986, "A Thermohydrodynamic Solution of Pivoted Thrust Pads: Part II—Static Loading," J. Tribol., **108**, pp. 208–213.

[7] Jeng, M. C., and Szeri, A. Z., 1986, "A Thermohydrodynamic Solution of Pivoted Thrust Pads: Part III - Linearized Force Coefficients," J. Tribol., **108**, pp. 214–218.

[8] Brockett, T. S., Barrett, L. E., and Allaire, P. E., 1996, "Thermoelastohydrodynamic Analysis of Fixed Geometry Thrust Bearings Including Runner Deformation," Tribol. Trans., **39**(3), pp. 555–562.

[9] Glavatskih, S. B., and Fillon, M., 2004, "TEHD Analysis of Thrust Bearings With PTFE-Faced Pads," *ASME/STLE International Joint Tribology Conference*, pp. 1–11.

[10] Ng, C. W., 1964, "Fluid Dynamic Foundation of Turbulent Lubrication Theory," ASLE Trans., **7**, pp. 311–321.

[11] Hirs, G. G., 1974, "A Systematic Study of Turbulent Film Flow," Asme J. Of Lubr. Technol., **96**, pp. 118–126.

[12] Wodtke, M., Fillon, M., Schubert, A., and Wasilczuk, M., 2012, "Study of the Influence of Heat Convection Coefficient on Predicted Performance of a Large Tilting-Pad Thrust Bearing," J. Tribol., **135**(2), p. 021702.

[13] Wasilczuk, M., and Rotta, G., 2008, "Modeling Lubricant Flow between Thrust-Bearing Pads," J. Tribol. Int., **41**(9-10), pp. 908–913.

[14] San Andrés, L., and Abdollahi, B., 2017, "A Computational Model For Tilting Pad Journal Bearings: Accounting For Thermally Induced Pad Deformations And Improving A Feed Groove Lubricant Thermal Mixing Model," Research Progress Report to the TAMU Turbomachinary Research Consortium,-TRC-B&C-01-17, Texas A&M University.

[15] Glavatskih, S., and Fillon, M., 2001, "TEHD Analysis of Tilting-Pad Thrust Bearings-Comparison with Experimental Data," *International Tribology Conference*, Japan Society of Tribologists, pp. 1579–1584.

[16] Glavatskih, S. B., Fillon, M., and Larsson, R., 2002, "The Significance of Oil Thermal Properties on the Performance of a Tilting-Pad Thrust Bearing," J. Tribol., **124**(2), pp. 377-385.

[17] Glavatskih, S. B., and Fillon, M., 2006, "TEHD Analysis of Thrust Bearings With PTFE-Faced Pads," J. Tribol., **128**(1), pp. 49-58.

[18] Ahmed, S. A, Fillon, M., and Maspeyrot, P., 2010, "Influence of Pad and Runner Mechanical Deformations on the Performance of a Hydrodynamic Fixed Geometry Thrust Bearing," Proc. Inst. Mech. Eng. Part J, J. Eng. Tribol., **224**(4), pp. 305–315.

[19] Nicholas, J. C., and Wygant, K. D., 1995, "Tilting Pad Journal Bearing Pivot Design For High Load Application," *Proceedings of the 24th Turbomachinery Symposium*, Vol. 1, pp. 33–37.

[20] Chen, W. J., 1995, "Bearing Dynamic Coefficients of Flexible-Pad Journal Bearings," Tribol. Trans., **38**(2), pp. 253-260.

APPENDIX A : DEFINITION OF ξ FUNCTIONS

Over a pad, ξ_i , i = 1: 4 are functions of the local viscosity (μ) across the fluid film, the thickness of the fluid film (h), and the intensity of the flow turbulence. Jeng et al. [5] state them as,

$$\xi_1(z) = \frac{(\frac{h}{2} - z)}{\mu_{(z)}\, f(\frac{z}{h})}\left[1 - \frac{g\left(\frac{z}{h}\right)}{f\left(\frac{z}{h}\right)}\right]$$

$$\xi_2(z) = \frac{1}{\mu_{(z)}\, f(\frac{z}{h})}\left[1 - \frac{g\left(\frac{z}{h}\right)}{f\left(\frac{z}{h}\right)}\right] \tag{44}$$

$$\xi_3(z) = \frac{(\frac{h}{2} - z)}{\mu_{(z)}\, f(\frac{z}{h})}$$

$$\xi_4(z) = \frac{1}{\mu_{(z)}\, f(\frac{z}{h})}$$

where μ is the fluid viscosity and f and g are the turbulence functions obtained based on Ng's modeling of flow turbulence phenomena [11].

$$f(z) = 1 + \frac{4}{10}\left[z\, h^{+}_{(r,\theta)} - 10.7 tanh\left(\frac{z\, h^{+}_{(r,\theta)}}{10.7}\right)\right]$$

$$g(z) = \frac{4}{10} z\, h^{+}_{(r,\theta)} \tanh\left(\frac{z\, h^{+}_{(r,\theta)}}{10.7}\right) \tag{45}$$

where h^{+} is a normalized film thickness defined as,

$$h^{+}_{(r,\theta)} = \frac{h_{(r,\theta)}}{\nu}\sqrt{\frac{1}{\rho}\frac{r\omega}{\int_0^h \frac{dz}{\mu\, f(r,\theta,z)}}} \tag{46}$$

According to the equation above, h^{+} also depends on the turbulence function *f(r,θ,z)*. Jeng et al. [5] introduce a method based on the local Reynolds number (Re_h) to estimate f

in Equation (46) and avoid an iterative search. The estimation for f is,

$$f\left(r,\theta,z\right)=\begin{cases} 2 & Re_h < 500 \\ 2-\left[\dfrac{800-Re_h}{300}\right]^{\frac{1}{8}} & 500 < Re_h < 800, \quad Re_h = \dfrac{r\Omega h}{\nu_{ave}} \\ 2 & 800 < Re_h \end{cases} \tag{47}$$

The fraction $\frac{\epsilon_m}{\nu}$, used in thermal energy transport equation (Eqn. (11)), is also a function of *f*,

$$\frac{\epsilon_m}{\nu}=(f-1)=\frac{4}{10}\left[z\ h^{+}_{(r,\theta)}-10.7tanh\left(\frac{z\ h^{+}_{(r,\theta)}}{10.7}\right)\right] \tag{48}$$

APPENDIX B : PIVOT STIFFNESS AND DAMPING CALCULATION

In general, pivot stiffness coefficients and damping coefficients are nonlinear functions of the applied load (force and moments) acting on a pad. However, considering small amplitude motions from equilibrium position allows the reaction force to be expressed as a linear function of pivot axial displacements and pad tilt motions.

$$\begin{bmatrix} F_{\eta_p} \\ M_{\gamma_p} \\ M_{\xi_p} \end{bmatrix} = \begin{bmatrix} F_{\eta_{p0}} \\ M_{\gamma_{p0}} \\ M_{\xi_{p0}} \end{bmatrix} - \begin{bmatrix} Z_{\eta e_{PS}} & Z_{\eta\alpha_S} & Z_{\eta\beta_S} \\ Z_{\gamma e_{PS}} & Z_{\gamma\alpha_S} & Z_{\gamma\beta_S} \\ Z_{\xi e_{PS}} & Z_{\xi\alpha_S} & Z_{\xi\beta_S} \end{bmatrix} \begin{Bmatrix} \Delta e_P \\ \Delta\alpha \\ \Delta\beta \end{Bmatrix} e^{i\omega t} \tag{49}$$

$Z_{XY_S}, (X = \gamma, \xi, \eta \text{ and } Y = e_P, \alpha, \beta)$ are structure pivot complex stiffness coefficients defined as,

$$\begin{bmatrix} Z_{\eta e_{PS}} & Z_{\eta\alpha_S} & Z_{\eta\beta_S} \\ Z_{\gamma e_{PS}} & Z_{\gamma\alpha_S} & Z_{\gamma\beta_S} \\ Z^k_{\xi e_{PS}} & Z_{\xi\alpha_S} & Z_{\xi\beta_S} \end{bmatrix} = \begin{bmatrix} K_{\eta e_{PS}} & K_{\eta\alpha_S} & K_{\eta\beta_S} \\ K_{\gamma e_{PS}} & K_{\gamma\alpha_S} & K_{\gamma\beta_S} \\ K_{\xi e_{PS}} & K_{\xi\alpha_S} & K_{\xi\beta_S} \end{bmatrix} + i\omega \begin{bmatrix} C_{\eta e_{PS}} & C_{\eta\alpha_S} & C_{\eta\beta_S} \\ C_{\gamma e_{PS}} & C_{\gamma\alpha_S} & C_{\gamma\beta_S} \\ C_{\xi e_{PS}} & C_{\xi\alpha_S} & C_{\xi\beta_S} \end{bmatrix} \tag{50}$$

The stiffness coefficient matric "*K*" relates to the type of a pivot and its configuration. Nicholas and Wygant [19] model pivot stiffness using an elasticity equation for solid on solid contact. The following summarizes the modeling for different type of pivots.

Spherical pivot (ball in cup): The pad is free to tilt around pivot (rotational stiffness are zero) and axial stiffness is modeled as an ideal point contact, i.e. [19]

$$K^k_{\eta e_{PS}} = 0.442\left(\frac{c_1 F_z}{{c_2}^2}\right)^{\frac{1}{3}}, \quad c_1 = \frac{D_h D_p}{D_h - D_p}, \quad c_2 = \frac{1-{\nu_p}^2}{E_p} + \frac{1-{\nu_h}^2}{E_h} \tag{51}$$

where F_z is the fluid film load acting the pad.

Cylindrical pivot (Cylinder in cylinder): This type of pivot allows for just 1D tilt, radial tilt angle "α", which reduces the system by 1 DOF. As a result, all parameters related to circumferential tilt angle "β" are disregarded. The model for an ideal contact line between two cylinders is [19]

$$K^{k}_{\eta e_{PS}} = 2\pi E_P \frac{\frac{L_C}{1-\nu_p{}^2}}{\frac{2}{3}+ln\left(\frac{16R_H R_P}{B^2}\right)}, \quad B=\left(16F_Z\frac{C_1}{L_C}E_P\right)^2, \quad C_1=\frac{D_H D_P}{(D_H-D_P)} \tag{52}$$

Flexure pivot: An idealized flexure pivot is modeled by treating it as cantilever beam with the pad as a lumped inertia at its free end [16]. For the case of TPTBs, the model for a flexure stiffness is

$$\mathbf{K}_{piv}=\begin{bmatrix} \frac{EA}{L} & 0 & 0 \\ 0 & \frac{4EI_\gamma}{L}-\frac{2F_Z L}{15} & 0 \\ 0 & 0 & \frac{4EI_\xi}{L}-\frac{2F_Z L}{15} \end{bmatrix} \tag{53}$$

where A, E and L are respectively the web cross-section area, web module of elasticity, and the length of the flexure web. I_γ and I_ξ are the web area moment of inertia with respect to (γ, ξ) axes.

Experimentally defined load-deflection curve: The pivot stiffness is a nonlinear function of pivot axial deflection,

$$K^{k}_{\eta e_{PS}} = A_0 + A_1\,\Delta e_P + A_2\,\Delta e_P{}^2 + A_3\,\Delta e_P{}^3 + A_4\,\Delta e_P{}^4 \tag{54}$$

where A_0 to A_4 are empirical parameters.

APPENDIX C : DETAILED PREDICTIONS OF THE COMPUTER PROGRAM

This appendix describes the graphical user interface (EXCEL GUI) for thrust bearings analysis, including "Nomenclature" spreadsheet, "Main TPTB" spreadsheet, and several spreadsheets containing performance predictions plotted versus load, speed, or clearance[1] (user choice). The "Main TPTB" spreadsheet includes two parts: parameter input form and performance prediction form. Figure 15 shows the parameter input form of the "Main TPTB" spreadsheet. The input form consists of 8 tables:

- **(1) Bearing geometry:**
  - Dimension of the bearing and pads. Use "Nomenclature" sheet for the definition of parameters.

- **(2) Fluid properties:**
  - Ambient pressure (P_a) is the pressure boundary condition at the trailing edge, inner radius, and outer radius of a pad (default = 0 bar).
  - Supply pressure (P_*) is the pressure boundary condition at the leading edge of a pad.
  - Cavitation pressure (P_c) is the pressure below which the fluid cavitates and does not generate hydrodynamic pressure (less than or equal to ambient pressure, default = 0 bar).
  - Supply temperature (T_*) is the temperature of the fresh lubricant fed to the bearing.
  - Density (ρ), specific heat (c_p), viscosity-temperature coefficient (α_{VT}), and thermal conductivity of the fluid (κ) are not a function of temperature (constant all over the fluid film domain).
  - Set the viscosity-temperature coefficient (α_{VT}) to zero for an isoviscous analysis, i.e. constant flow viscosity.

- **(3) Thermal properties:**
  - Pad thermal conductivity (κ_p) and pad heat convection coefficient (λ) are constant all over the fluid film domain (not functions of pad temperature).
  - Thermal carry-over coefficient (λ_{mix}) is the fraction of hot oil going from one pad to the next (an empirical parameter).

[1] Note that the term clearance refers to the fluid film thickness at the pivot location of a pad.

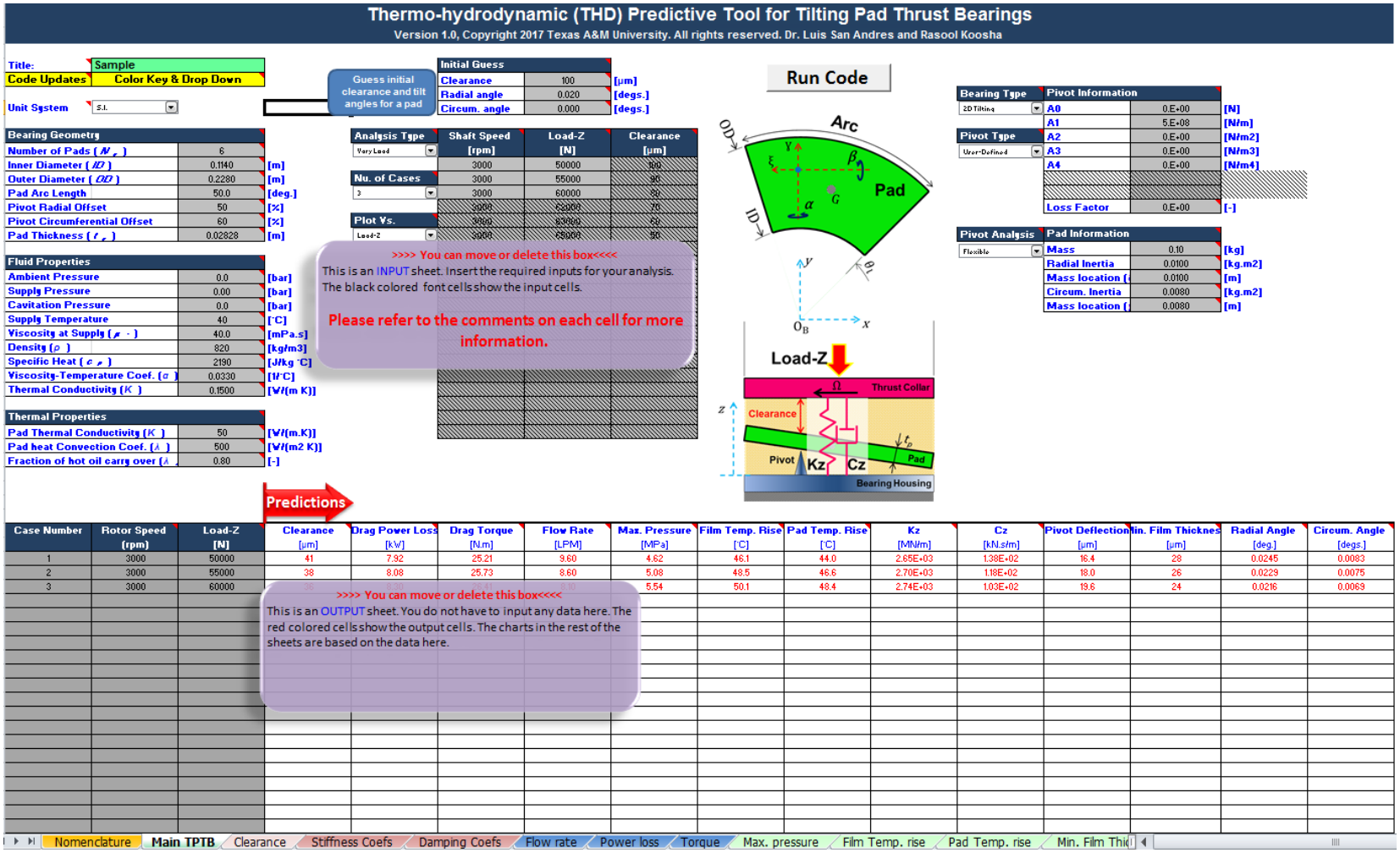

Figure 15. Graphical user interface (GUI) for thrust bearings, parameter input section and the prediction table.

- **(4) Operating condition:**
    - Include two choice of analysis type:

        1) Load vary: Determines an equivalent clearance based on the shaft speed and the applied load. The code requires initial values for clearance (h_P) and pad tilt angles (α,β) to start from.

        2) Clearance vary: Determines the hydrodynamic reaction force generated in the bearing based on the shaft speed and clearance. The code requires initial values for pad tilt angles (α,β) to start from.

    - Note that, in the GUI, the fluid film thickness at the pivot location, called clearance, is selected as a characteristic value for the fluid film thickness on a pad.
    - The user can choose for predictions to be plotted versus shaft speed, and load or clearance (based on the choice of analysis).

- **(5) Pivot Information:**
    - Bearing type:

        Fixed geometry: The pads are fixed (no tilting). The initial values for pad tilt angles (α,β) remain same.

        1D tilting: The pads only tilt around ɣ-axis. The initial values for pad circumferential tilt angle (β) remains same. The code predicts the equilibrium position for pad radial angle (α).

        2D tilting: The code predicts the tilt angles (α,β) for the pad equilibrium position.

    - The content of Table (5) varies based on the bearing type, the choice of pivot stiffness theory (Herts theory of elastic contact, user defined load-deflection curve, or flexure pivot), and the choice of pivot analysis (rigid or flexible).

- **(6) Pad information:**
    - Pivot analysis:
      Rigid: Pivot stiffness is not included in the frequency model. The pivot deflection values in the prediction table return as zero.

Flexible: Pivot stiffness is included in the frequency reduced model (the user must input mass of a pad, its mass moment of inertia with respect to (γ,ξ) axes, and location of mass center).

- The content of Table (6) varies base on the choice of pivot analysis and the bearing type.

- **(7) Grids:**
  - The user has the choice to either manually input a proper number of nodes for the computation process or leave it to the code to automatically grid the domain (the fluid film and a pad).
  - If manual, the user must limit the total number of nodes to 16000 for each domain (a pad or the fluid film).
  - If automatic, three choices are available for mesh size:

    1) Fine size: circumferential grid size is equal to 1 deg.

    2) Medium size: circumferential grid size is equal to 2 deg.

    3) Rough size: circumferential grid size is equal to 3 deg.

    The ratio of circumferential/radial grid size is approximately equal to 1 for all choices. The ratio of circumferential/axial grid size in a pad is also approximately equal to 1. Number of nodes cross the fluid film is equal to1/2 of number of nodes in the circumferential direction.

- **(8) Initial guess:**
  - The initial guess for bearing clearance is only required if the code solves for an equilibrium film thickness (load vary).
  - The initial guess for circumferential tilt angle (β) remains same for fixed geometry and 1D tilting bearings.
  - The initial guess for circumferential tilt angle (α) remains same for fixed geometry thrust bearings.

The prediction table includes columns for drag power loss, friction torque, flow rate, maximum pressure, maximum fluid film temperature, maximum pad temperature, bearing stiffness and damping coefficients ([K,C]), and etc.

The “Main TPTB” spreadsheet also includes plots for the predicted fluid film thickness, hydrodynamic pressure field, 3D fluid film temperature, and 3D pad temperature (See Figure 16).

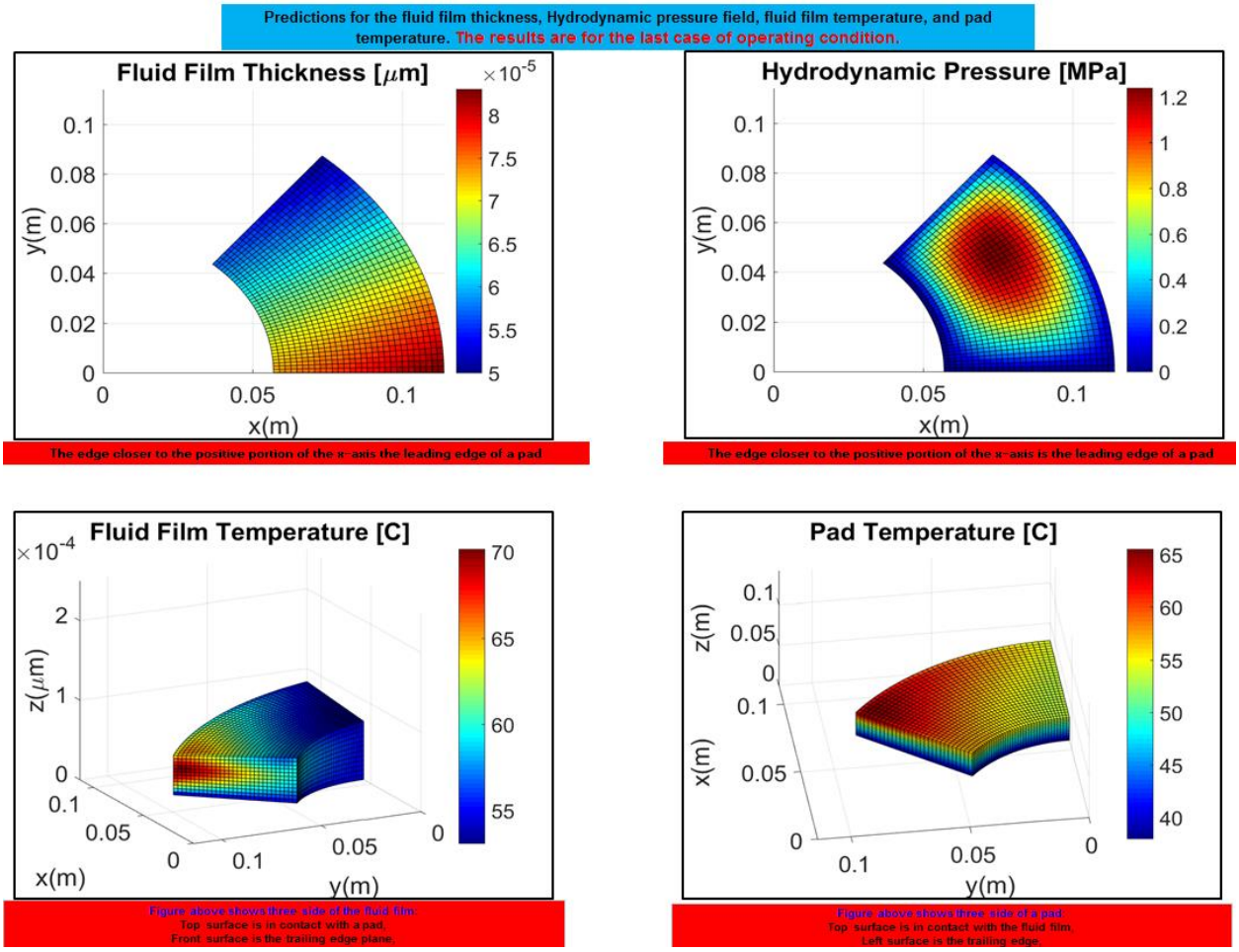

Figure 16. Graphical user interface (GUI) for thrust bearings, graphs of predictions for fluid film thickness, hydrodynamic pressure field, 3D fluid film temperature, and 3D pad temperature.